Transport properties of graphene containing structural defects

Aurélien Lherbier,[1] Simon M.-M. Dubois,[2] Xavier Declerck,[1] Yann-Michel Niquet,[3]
Stephan Roche,[4,5] and Jean-Christophe Charlier[1]

[1]*Université Catholique de Louvain (UCL), Institute of Condensed Matter and Nanoscience (IMCN), Chemin des étoiles 8, 1348 Louvain-la-Neuve, Belgium*

[2]*University of Cambridge, Cavendish Laboratory, Theory of Condensed Matter group, JJ Thomson Avenue, Cambridge CB3 0HE, United Kingdom*

[3]*CEA-UJF, INAC, SP2M/L_Sim, 17 rue des Martyrs, 38054 Grenoble Cedex 9, France*

[4]*CIN2 (ICN-CSIC) and Universitat Autonoma de Barcelona, Catalan Institute of Nanotechnology, Campus de la UAB, 08193 Bellaterra (Barcelona), Spain*

[5]*Institució Catalana de Recerca i Estudis Avançats (ICREA), 08010 Barcelona, Spain*

(Received 29 March 2012; published 1 August 2012)

We propose an extensive report on the simulation of electronic transport in two-dimensional graphene in presence of structural defects. Amongst the large variety of such defects in sp^2 carbon-based materials, we focus on the Stone-Wales defect and on two divacancy-type reconstructed defects. Based on *ab initio* calculations, a *tight-binding* model is derived to describe the electronic structure of these defects. Semiclassical transport properties including the elastic mean-free paths, mobilities, and conductivities are computed using an order-N real-space Kubo-Greenwood method. A *plateau* of minimum conductivity ($\sigma_{sc}^{min} = 4e^2/\pi h$) is progressively observed as the density of defects increases. This saturation of the decay of conductivity to σ_{sc}^{min} is associated with defect-dependent resonance energies. Finally, localization phenomena are captured beyond the semiclassical regime. An Anderson transition is predicted with localization lengths of the order of tens of nanometers for defect densities around 1%.

DOI: 10.1103/PhysRevB.86.075402 PACS number(s): 73.23.−b, 72.15.Rn, 72.80.Vp, 71.23.An

I. INTRODUCTION

Graphene, a one-atom-thick layer of carbon atoms packed in a two-dimensional (2D) honeycomb lattice, was first isolated in 2004 (Ref. 1) and rapidly turned out to be a very attractive material.[2] Over the past few years, it has demonstrated exceptional mechanical, optical, thermal, electronic, and transport properties and offered significant insights into fundamental quantum physics.[3] The existence of a linear conical dispersion relation for electrons near the Fermi energy implies that low-energy carriers behave as massless Dirac fermions.[4] The bipartite nature of the carbon honeycomb lattice in graphene is at the origin of a pseudospin degree of freedom. This pseudospin combined with the valley degeneracy confers to the wave function a highly symmetric nature responsible for a forbidden intravalley scattering, a π Berry phase,[5] and other features such as weak antilocalization properties.[6–8]

Besides, graphene is expected to be a material of choice for future nanoelectronics. Indeed, it exhibits an extremely high stability and a thermal conductivity predicted to be twice that of diamond. Graphene shows a large response to perpendicular electric fields allowing to tune the type and concentration of charge carriers. Its high carrier mobilities[9] and long phase coherence length[10] suggest potential applications in integrated circuits, high-mobility transistors, or single-molecule gas sensors. Eventually, graphene can also be patterned using existing lithographic techniques and meets many requirements for the process and design of nanoelectronic devices.

However, the lack of electronic (or transport) gap in pristine graphene is an issue that has to be overcome in order to achieve high I_{on}/I_{off} current ratio in graphene-based field-effect devices.[11] In this context, controlled defects engineering in sp^2 carbon-based materials have become a topic of great excitement.[12] Indeed, the electronic (and transport) properties of carbon nanotubes[13] and graphene-based materials[14–16] can be considerably enriched by chemical modifications, including substitution and molecular doping[17,18] as well as functionalization. Another approach to tune graphene's properties is provided by ion or electron beam irradiation, which introduces structural defects (e.g., vacancies) in sp^2 carbon-based nanostructures. As an example, convincing room-temperature signatures of an Anderson regime in Ar^+-irradiated carbon nanotubes have been reported.[19,20] In contrast, the conductivity of irradiated graphene samples saturates at the Dirac point above e^2/h even down to cryogenic temperatures,[21] suggesting somehow a stronger robustness of graphene with regards to structural defects.

In this paper, the Kubo-Greenwood methodology combined with the scaling theory of localization is used in order to investigate the localization phenomena in defective graphene. A strong (Anderson) localization regime is observed in defective graphene, but only in energy windows corresponding to specific resonances associated with certain types of structural defects. Depending on the structural defects, these energy windows may or may not coincide with the Dirac point.

In Sec. II, the geometry and the electronic properties of structural defects are described within a combined *ab initio* and *tight-binding* technique. In Sec. III, the real-space Kubo-Greenwood methodology is presented and the transport properties of large graphene planes with a realistic structural disorder are discussed. An in-depth analysis of the localization phenomena obtained within the present approach is also performed. Eventually, our results are summarized in Sec. IV and the possibility to experimentally validate our theoretical predictions is discussed.

II. ELECTRONIC PROPERTIES OF STRUCTURAL DEFECTS

A. Geometry of structural defects

Structural defects exist in various forms in graphene[22–25] and more generally in all sp^2 carbon-based materials. In this paper, three types of structural defects are considered: the Stone-Wales (SW) defect and two possible reconstructions of the divacancy defect. These three defects are nonmagnetic, in contrast with monovacancies, for instance, which contain an unbounded carbon atom. Consequently, the issue of induced magnetization[26] and possible spin interaction between defects is not present in this study. The SW defect is a well-known and common defect in sp^2 carbon-based materials, which consists in a 90° rotation of a carbon-carbon bond.[27] This topological transformation yields to the formation of two heptagons connected with two pentagons [Fig. 1(a)]. Ma *et al.* have reported in a theoretical study[28] that in graphene a SW defect could produce a slight out-of-plane deformation. In this situation, the carbon bonds in the close neighboring of the SW defect are no more fully sp^2 hybridized but become partially sp^3-like hybridized. Considering this theoretical prediction would imply that the new orbital hybridization could induce spin-orbit coupling as it has been predicted for the case of ripples.[29] However, such out-of-plane deformations have never been obtained in our calculations. To ensure that the in-plane geometry was not a metastable state related to a local minimum of total energy, additional calculations have been performed with a starting geometry containing out-of-plane atoms. After structural relaxation, the out-of-plane atoms always go back to the plane. Moreover, to our knowledge, no experimental scanning tunneling microscopy (STM) images have confirmed the behavior predicted in Ref. 28. Therefore, only the in-plane geometry has been considered in this paper.

Vacancies are missing carbon atoms in the honeycomb lattice. They can not be considered as a reversible geometrical modification of the ideal graphene plane and thus, strictly speaking, they do not belong to the class of topological defects. Vacancies can be created by irradiating the graphene plane with ions such as Ar^+ for instance. Single vacancies (or monovacancies) migrate easily in the graphene plane and are stabilized when they recombine with another one to give a divacancy defect.[12,30,31] Two kinds of divacancy defects are explored here. In the first case, the reconstruction yields to the formation of two pentagons and one octagon [so-called 585, Fig. 1(b)], while in the second case it yields to the formation of three pentagons and three heptagons [so-called 555-777, Fig. 1(c)]. According to our *ab initio* calculations, the formation energy of the 555-777 divacancy is smaller than the one of the 585 divacancy by about 0.9 eV. This stabilization of the 555-777 divacancy with regards to the 585 divacancy in graphene, which contrasts to the case of carbon nanotubes, is also reported by Lee *et al.*[30] A third kind of divacancy, not studied here, has also been reported.[22,32] This third type of divacancy has a larger extension and is thus more complicated to parametrize within a *tight-binding* model. Actually, it involves nine carbon rings including four pentagons (one hexagon and four heptagons) (so-called 5555-6-7777). To conclude on the description of the geometry of these defects, one notes that the 585 divacancy as well as the SW defect possess a D_{2h} symmetry since two orthogonal symmetry axes can be defined, whereas the 555-777 divacancy possesses a D_{3h} symmetry (see Fig. 1). The presence of these three structural defects has already been experimentally reported in graphene by means of STM experiments[14,33] or transmission electron microscopy (TEM) images,[32] and their influence on the transport properties deserves in-depth inspection.

B. *Ab initio* simulations

In order to study these three defects, *ab initio* simulations are first employed. The calculations have been performed using the SIESTA package[34] in the generalized gradient approximation (GGA) for the exchange-correlation functional in the Ceperley-Alder form,[35] as parametrized by Perdew and Zunger.[36] Troullier-Martins pseudopotentials are used to account for the core electrons.[37] The valence electron wave functions are expanded in a double-ζ polarized basis set of finite-range numerical pseudoatomic orbitals.[38] The *ab initio* calculations have two objectives. On one hand, it allows us to obtain the detailed geometry of the defect, and on the other hand, it allows us to elaborate a *tight-binding* model for an isolated defect. In both cases, a convergence study with regards to the size of the cell used in calculations is required. The supercell technique, which consists in placing the defect in a cell being a multiple of the standard unit cell of the pristine system, is therefore employed.

First, a structural relaxation of the supercell containing one defect is performed for different supercell sizes, i.e., 4×4, 5×5, 6×6, and 7×7 (1×1 being the conventional unit cell). To ensure that the defect does not interact with its repeated images, the potential associated to the defect must tend to zero at the edges of the supercell. The 7×7 supercells are found to be large enough for each defect to obtain such a convergence. Relaxed positions of the atoms in the vicinity of the defects are then extracted and will be used to construct the *tight-binding* models. The relaxed geometry of each defect in 7×7 supercells is displayed in Fig. 1. The SW defect does not induce strong distortions of the neighboring hexagon rings, whereas the 585 divacancy exhibits a more pronounced

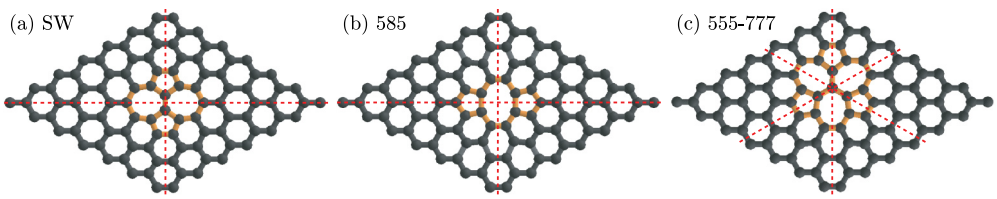

FIG. 1. (Color online) Schematic of the three structural defects: (a) Stone-Wales, (b) 585, and (c) 555-777 divacancies. Symmetry axes are drawn in red dashed lines.

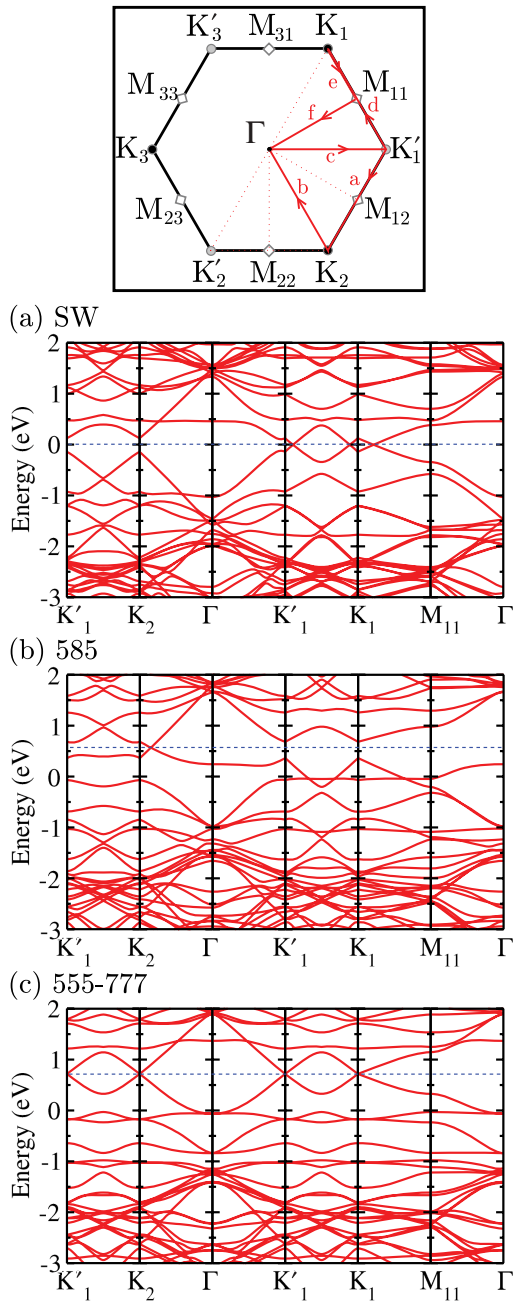

FIG. 2. (Color online) Electronic band structures computed using the SIESTA package along high-symmetry lines in the Brillouin zone (top panel) for 7 × 7 supercell containing (a) one SW defect, (b) one 585 divacancy, (c) one 555-777 divacancy. The Fermi energy is set to zero and the Dirac energy is indicated with a horizontal blue dashed line.

impact. Indeed, in the latter case, a distortion of the hexagon rings along the vertical axis (aligned with octagon) is observed. A slighter distortion is observed for the 555-777 divacancy.

In Fig. 2, the electronic properties of the defects are examined through the study of their respective band structures. The electronic bands are plotted along an extended path connecting high-symmetry points in the Brillouin zone. The path used here (see top panel of Fig. 2), which is longer than the usual K-Γ-M-K path used for graphene, has been carefully chosen to evidence all useful details. Indeed, as the structural defects break the symmetry of the pristine graphene lattice,[39] the hexagonal symmetry of the Brillouin zone is also lifted. As a consequence, paths in the Brillouin zone that were equivalent in the pristine case can become inequivalent when such a type of defect is introduced. By definition, if there are no other symmetries apart from the time-reversal symmetry, half of the Brillouin zone needs to be examined, which implies at least 10 branches (full and dotted red lines in top panel of Fig. 2). Here, a minimal continuous path composed of six branches has been chosen in order to depict all important details for each defect. This extended path is labeled *a*-*b*-*c*-*d*-*e*-*f* in the top panel of Fig. 2.

Then, for sake of comparison between band structures of the three defects, the Fermi energy has been set to zero and the energy associated with the Dirac point has been indicated by a horizontal blue dashed line. The Dirac cone band crossing occurs at an energy $E = 0.7$ eV above the Fermi energy in case of the 555-777 divacancy [Fig. 2(c)], thus suggesting that this defect has a p-type doping character since the Fermi energy has been shifted below the Dirac point energy, whereas both energies were aligned in the pristine case. Obviously, the magnitude of the shift of the Fermi energy is related to the concentration of defects (n_d). One defect in a 7×7 supercell corresponds to $n_d \sim 3.9 \times 10^{13}$ cm^{-2} or, equivalently, $n_d \sim 1\%$, which is the maximum concentration that will be considered in Sec. III for transport properties. For the 585 divacancy [Fig. 2(b)], the Dirac point energy is located at $E = 0.6$ eV above the Fermi energy, also implying a p-type doping character although slightly weaker than for the 555-777 divacancy. Finally, the Dirac point energy and the Fermi energy are both aligned in case of a SW defect [Fig. 2(a)], which indicates a no-doping effect.

As mentioned in the previous paragraph, the 555-777 divacancy possesses a D_{3h} symmetry, which is the same symmetry group as a single Dirac cone (at K or at K'). Indeed, even if very close to the Dirac point energy the Dirac cone is isotropic, at higher energies it has been demonstrated theoretically[40,41] and by angle-resolved photoemission spectroscopy (ARPES) measurements[42] that a trigonal warping emerges. This effect is a signature of the D_{3h} symmetry of a single Dirac cone related to the existence of two inequivalent triangular sublattices. Since the 555-777 divacancy has the same symmetry, the band structure of the defected system preserves the initial symmetry present in pristine graphene. Therefore, the usual electronic path composed of only three branches should be sufficient. It is actually easy to see, for instance, that in Fig. 2(c), paths Γ-K_2 and Γ-K'_1 are equivalent as well as paths K'_1-K_2 and K'_1-K_1. On the contrary, the 585 divacancy and the SW defect possess a D_{2h} symmetry which breaks the symmetry of the Dirac cone and as a consequence the latter is shifted. For the 585 divacancy, the first Dirac cone band crossing corresponding to K valley is shifted along the direction $K_2 \rightarrow \Gamma$, whereas the second Dirac cone band crossing corresponding to the K' valley is shifted in the opposite direction ($K'_3 \rightarrow \Gamma$). The latter is not visible in Fig. 2(b) since the path K'_3-Γ is not represented (but is the symmetric of K_2-Γ). For the SW defect, the shift is reversed, i.e., the first Dirac cone band crossing corresponding to the K valley is shifted along the direction $\Gamma \rightarrow K_2$ (or

equivalently along $K_1 \rightarrow K_1^{'}$), whereas the second Dirac cone band crossing corresponding to the $K^{'}$ valley is shifted along the opposite direction ($K_1^{'} \rightarrow K_1$). For both defects, paths Γ-K_2 and Γ-$K_1^{'}$ are now inequivalent as well as paths $K_1^{'}$-K_2 and $K_1^{'}$-K_1. This shift of the Dirac cone induced by symmetry breaking has already been reported in case of uniaxial strain,[43] but to our knowledge not in case of point defects.

Some features of the transport properties could already be anticipated from these electronic-band-structures analyses. For instance, rather flat bands close to the Dirac point energy are observed. These flat bands have to be related to the presence of the defect, and can be seen as resonance energies associated with electrons localized around the defect. Such localized states are in general responsible of reduced transport properties. For the SW defect, a flat band is observed around $E = 0.5$ eV above the Dirac point energy. A second flat band is located at $E = -1.75$ eV, but is embedded in many dispersive bands. For the 585 divacancy, two regions of flat bands are observed around 0 and 0.25 eV corresponding, respectively, to energies $E \sim -0.6$ eV and $E \sim -0.35$ eV below the Dirac point energy. Another flat band is also observed around -1 eV, but again many other dispersive bands stand at this energy. Finally, for the 555-777 divacancy, much more flat-band regions are observed but far away from the Dirac point energy. Indeed, flat bands are observed around 1.35, 0, and -1 eV, which correspond, respectively, to energies $E = 0.45$ eV above the Dirac point energy, $E = -0.7$ and -1.7 eV below the Dirac point energy.

Finally, one concludes the analysis of band structures by investigating the case of charged systems. This is reported here as a validation of the rigid-band model that will be used in the next section in order to discuss transport properties of defective graphene at different energies. In contrast with the experimental configuration where an applied gate voltage can effectively fill or deplete the active part of the device with electrons, our transport model relies on the rigid shift of the Fermi energy in order to describe out-of-equilibrium situations. Indeed, the tight-binding and transport models presented in the next paragraphs are essentially a model of the equilibrium case and can not account for the detailed impact of the excess of charge. In Fig. 3, the validity of this rigid-band approximation, which neglects these charge effects, is verified by looking at the impact of net charges on the electronic band structures. Calculations have been performed for systems with excess charge of $\{-3, -2, -1, +1, +2, +3\}\ |e|$ where e is the elementary charge. Note that, computationally, the added charges are compensated by a background jellium. For a 7×7 supercell, a charge of $3\ |e|$ corresponds to a carrier density of $n \sim 1.2 \times 10^{14}$ cm^{-2}. Figure 3 shows that the overall band structure is not strongly modified by the added charges up to $\pm 3\ |e|$, especially in the region $[-1, +1]$ eV around the Fermi energy. For higher energies, the approximation of rigid-band model is more questionable. Also, it is interesting to note that, when the conventional path composed of three branches (Γ-K-M-Γ) in the Brillouin zone is used to plot the band structure, a fictitious energy gap is observed (see Fig. 3). This pinpoints the importance of the symmetry-breaking mechanisms occurring in the Brillouin zone and the need of such an extended path as used in Fig. 2.

C. Tight-binding models

The tight-binding (TB) models for pristine graphene and for the three defects are derived from the previous *ab initio* calculations. A common way to obtain the TB parameters is to choose a set of points $E(k)$ in the *ab initio* (or experimental) band structure and then to use them as constraints in a fit procedure (based on gene algorithm for instance). The TB parameters are adjusted by the fit to reproduce the full band structure as well as possible. Here, a different strategy is applied. Since the SIESTA Hamiltonian is expressed in a localized orbitals basis set, the TB parameters can be directly *extracted* by performing successive operations on this SIESTA Hamiltonian. In particular, the basis set has to be reduced to a single p_z orbitals orthogonal basis. The details of the technique will be presented in a separate paper.[44]

Most TB studies use a first-nearest-neighbors π-π^* TB model to describe graphene electronic properties. However, in this work, a two-center third-nearest-neighbors π-π^* orthogonal TB model has been chosen. Indeed, already for pristine graphene, a third-nearest-neighbors π-π^* model gives much more reasonable results since it allows in particular to recover the existing asymmetry between valence (π) and conduction (π^*) bands. In contrast, a first-nearest-neighbors π-π^* model produces a totally symmetric band structure as shown in Fig. 4. The comparison between the *ab initio* and the third-nearest-neighbors model band structures and total densities of states (DOS) is very satisfactory. However, the K-M branch in the conduction-band side remains not exactly reproduced by this third-nearest-neighbors model. The TB parameters of this model are composed of a single onsite term ε_{p_z} and three hopping terms γ_0^1, γ_0^2, and γ_0^3 corresponding, respectively, to first, second, and third nearest neighbors. The pristine graphene Hamiltonian then reads as

$$H = \sum_i \langle \phi_i | \varepsilon_{p_z} | \phi_i \rangle + \sum_{i,\langle j,k,l \rangle} \big(\langle \phi_i | \gamma_0^1 | \phi_j \rangle + \langle \phi_i | \gamma_0^2 | \phi_k \rangle + \langle \phi_i | \gamma_0^3 | \phi_l \rangle \big) \quad (1)$$

with $\varepsilon_{p_z} = 0.597\,45$ eV and $\gamma_0^1 = -3.093\,30$ eV, $\gamma_0^2 = 0.199\,15$ eV, $\gamma_0^3 = -0.162\,14$ eV. The sums on index i run over all carbon p_z orbitals. The sums over j,k,l indices run over all p_z orbitals corresponding, respectively, to first, second, and third nearest neighbors of the ith p_z orbital.

To obtain the local TB parameters corresponding to the defect potential, the same extraction techniques as for the pristine graphene have been used. In the defect potential, only onsite modifications have been considered, but the new arrangement of neighbors for carbon atoms in the core of the defects has also been carefully taken into account. In case of the SW defect, for instance, the rotation of the carbon-carbon bond yields to a modification of first, second, and third nearest neighbors for carbon atoms in the vicinity of the rotated bond. To check the validity of the TB parametrization of the defects, the *ab initio* and the TB band structures have been compared for a 7×7 supercell containing one defect. In Fig. 5, the TB band structure (black dotted lines) is superimposed with the *ab initio* band structure (red full lines) already reported in Fig. 2. A good agreement is obtained especially for the valence bands. The conduction-band side seems to be less accurate, but this

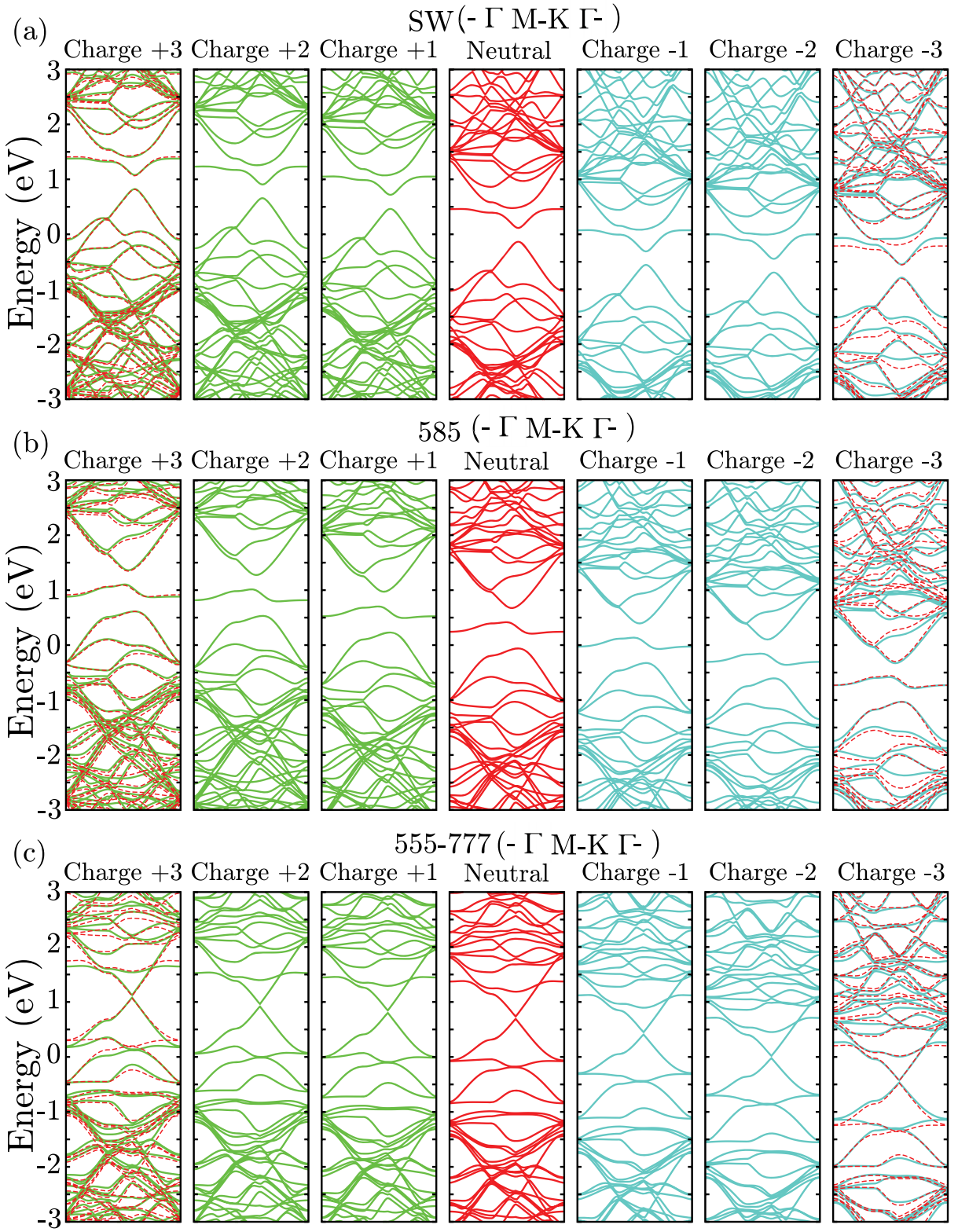

FIG. 3. (Color online) Electronic band structures computed using the SIESTA package along high-symmetry lines Γ-M-K-Γ for 7×7 supercell containing (a) one SW defect, (b) one 585 divacancy, (c) one 555-777 divacancy, and with different excess charge ($\{-3, -2, -1, +1, +2, +3\}\ |e|$). The Fermi energy is set to zero. The band structures of positively, neutral, and negatively charged systems are plotted, respectively, with green, red, and blue lines. To evidence the rigid-band approximation, the shifted neutral band structure is also reported in dashed red lines in case of an excess charge of $-3, +3|e|$.

is uniquely due to the inability of the pristine graphene TB model to reproduce conduction band along the K-M branch, as already illustrated in Fig. 4. As a consequence, some of the conduction bands are shifted to higher energies. A comparison

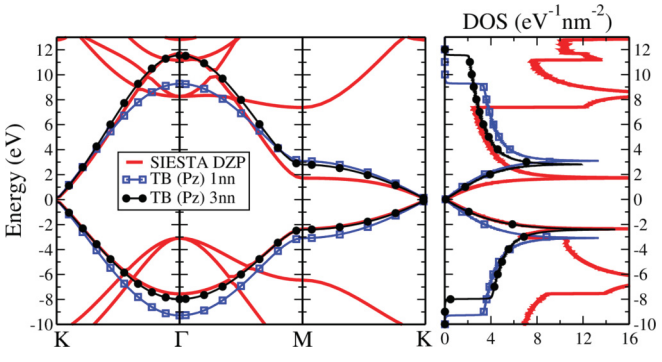

FIG. 4. (Color online) Electronic band structures and corresponding density of states (DOS) computed using the SIESTA package with a double-ζ polarized (DZP) basis set (red lines) along the K-Γ-M-K path for 1×1 supercell (unit cell). The TB band structures for a first-nearest-neighbors model (1 nn, blue lines with open square symbols) and for a third-nearest-neighbors model (3 nn, black lines with filled circle symbols) are also plotted. The Fermi energy is set to zero.

of *ab initio* and TB DOS is also provided in the right panels of Fig. 5.

III. TRANSPORT PROPERTIES

In this section, the transport properties of large defective graphene planes are investigated. Although the study of the supercell electronic structure performed in the prior section allows us to draw some preliminary conclusions on the impact of structural defects on transport, the randomness character of a realistic disorder at the mesoscopic scale has to be taken into account. Therefore, based on the developed TB models for isolated defects, large graphene planes containing randomly distributed defects of various nature and density are built (Fig. 6). It is important to pay attention to the various possible orientations of the defects. As explained previously, the structural defects possess specific symmetry groups smaller than the one of the honeycomb lattice. Thereby, for the SW and the 585 divacancy, three possible orientations exist, whereas there are only two for the 555-777 divacancy. If a given orientation was over represented, anisotropic transport properties would be observed. In our disorder model, the defects are randomly oriented to avoid this effect. In a previous paper, the case of graphene planes containing different densities of only one type of defect has been investigated.[45] In the next paragraph, the case of graphene planes containing a *mixture* of defects is studied in order to be as close as possible to the experimental situation.

A. Density of states

Before achieving an in-depth analysis of the transport properties, a first insight of transport features can be obtained by examining the density of states of randomly disordered graphene planes as it has been performed in Sec. II B for the band structures and the DOS of defects in small supercells. Here, the DOS of much larger graphene planes with randomly distributed defects reveal the salient features that persist after taking into account the randomness character of the disorder. In Fig. 7, the total DOS of large graphene planes containing $n_d = 1\%$ of SW, 585, and 555-777 divacancies, computed using the recursion method,[46] is compared with the total DOS previously obtained for a 7×7 supercell containing one defect ($n_d \sim 1\%$). A first observation is that the DOS of randomly disordered systems is much smoother than the one corresponding to a supercell.[47] In the random case, most of the peaks have disappeared except the ones close to the Dirac point (in Fig. 7, the Dirac point has been set to zero.). The broadening due to the random distribution disorder is more efficient in energy regions containing a lot of bands. Close to the Dirac point, the quantity of bands is less dense, preserving the defect-induced resonances. The presence of such resonant states induced by local defects is a well-known issue.[24,45,48–51] Second, the positions of these persisting resonance energy peaks corroborate the previous analysis carried out on supercell band structures. The DOS of randomly disordered graphene planes confirm that the electron transport in an energy region around $E = 0.35$ eV is expected to be degraded for SW defects, whereas hole transport should be altered around $E = -0.35$ eV for 585 divacancies, and finally that 555-777 divacancies exhibit several resonant energies around $E = 0.6, -0.8, -2.1$ eV, which should also lead to reduced transport performances.

The case of a mixture of defects is now explored by considering graphene planes containing half SW/half 585 divacancy (SW/585), then half SW/half 555-777 divacancy (SW/555-777), and finally half 585/half 555-777 divacancies (585/555-777). The corresponding DOS of these systems for $n_d = 1\%$ of defects in total are plotted in Fig. 8. These DOS of graphene planes containing a mixture of two types of defects are compared also with the DOS of graphene planes containing a single type of defect separately (i.e., $n_d = 0.5\%$). It is obvious that the features observed in the DOS of the mixed systems are roughly the sum of the individual features of each defect type. The particular case of SW/585 is interesting in the sense that the resonance peaks of these two defects are almost symmetric with respect to the Dirac point. Moreover, since the resonance peaks are relatively close to the initial Dirac point, they tend to overlap and yield to an increase of the DOS at the Dirac point. In this special situation, there is no more a clear minimum of DOS associated with the Dirac point. By adding other types of defects, a large increase of the DOS at the Dirac point can be foreseen. This is actually what is observed for highly defective or *amorphous* graphene membranes.[52–54] But, this increase of DOS comes from resonant states mainly localized around the defects which will therefore not participate to the transport of charge carriers, but will rather degrade it.

B. Kubo-Greenwood methodology

The transport properties of large graphene planes containing structural defects are calculated using an efficient real-space order-N Kubo-Greenwood method.[55–60] This very efficient technique gives a direct access to the main transport quantities in the semiclassical regime as well as in the quantum regime in which all multiple scattering events and interferences are retained. All quantities at energy E are extracted from the wave-packet dynamics. The latter is characterized by

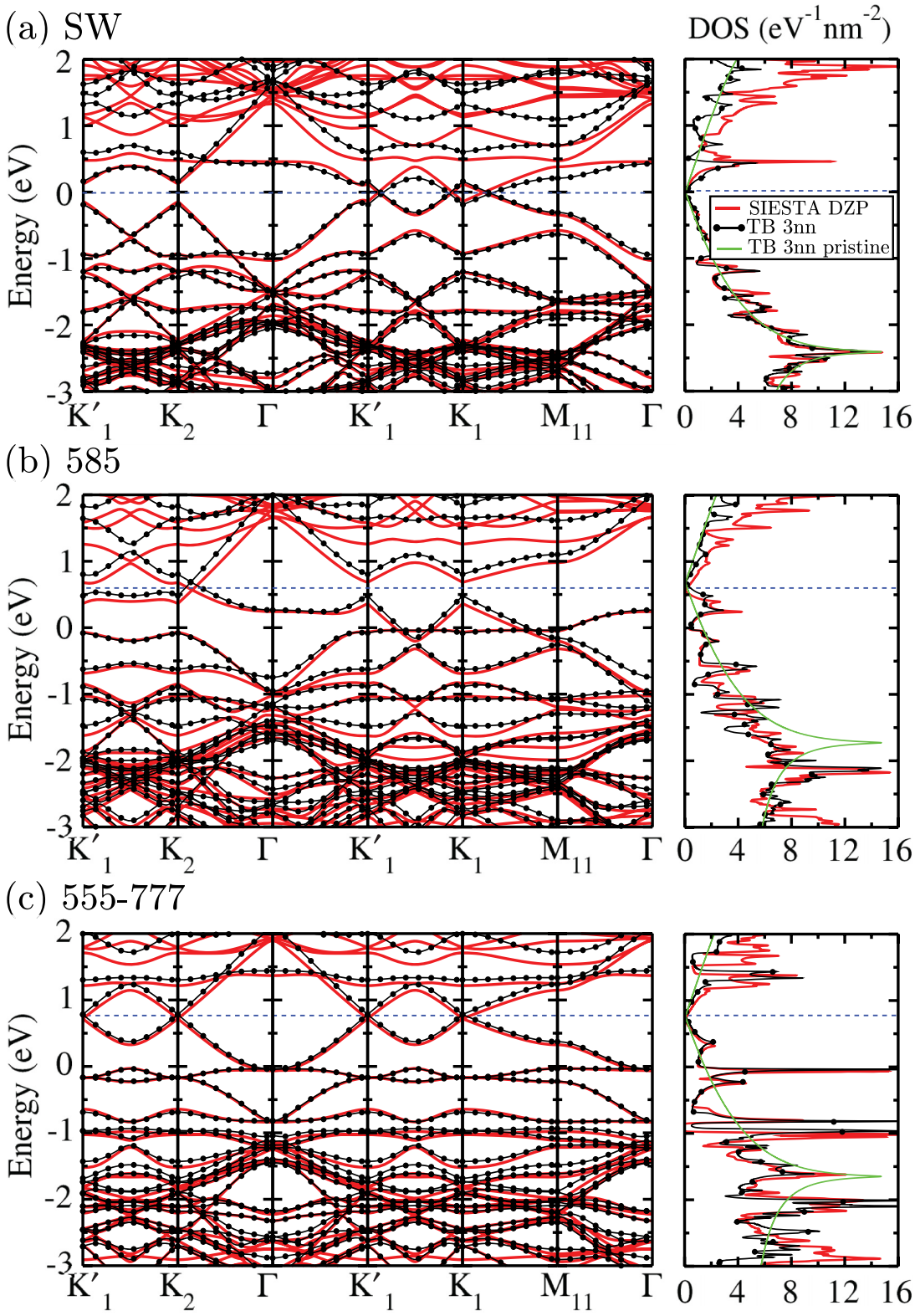

FIG. 5. (Color online) *Ab initio* electronic band structure (red lines) computed using SIESTA with a double-ζ polarized (DZP) basis set along high-symmetry lines in the Brillouin zone (see left panel of Fig. 2) for 7×7 supercell containing (a) one SW defect, (b) one 585 divacancy, (c) one 555-777 divacancy. The TB band structures for a third-nearest-neighbors model (3 nn, black lines with filled circle symbols) is also plotted. The Fermi energy is set to zero and the energy of the Dirac point is indicated with a horizontal blue dashed line. In the right panels, the corresponding DOS are plotted. The pristine graphene DOS for a third-nearest-neighbors model is superimposed for sake of comparison (green thin lines).

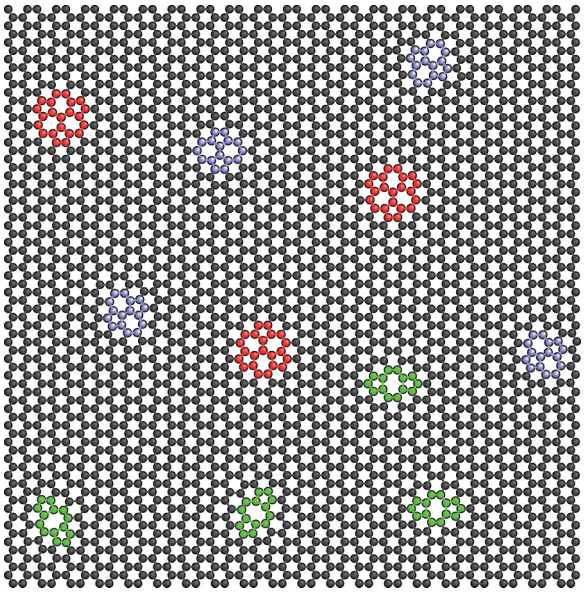

FIG. 6. (Color online) Example of a small piece of defected graphene plane generated using the TB models developed for the three defects. Both position and orientation of the defects are chosen randomly.

the time-dependent diffusivity $D(E,t) = \Delta R^2(E,t)/t$ where $\Delta R^2 = \Delta X^2 + \Delta Y^2$ is the mean quadratic spreading of wave packets. The mean quadratic spreading along a given direction is evaluated from the Hamiltonian and the corresponding position operator as $\Delta X^2(E,t) = \mathrm{Tr}[\delta(E-\hat{H})|\hat{X}(t) - \hat{X}(0)|^2]/\mathrm{Tr}[\delta(E-\hat{H})]$. Tr is the trace over p_z orbitals and $\mathrm{Tr}[\delta(E-\hat{H})]/S = \rho(E)$ is the total DOS (per unit of surface). The two position operators $\hat{X}(t)$ and $\hat{Y}(t)$ are expressed in the Heisenberg representation $[\hat{X}(t) = \hat{U}^\dagger(t)\hat{X}(0)\hat{U}(t)]$ and the time evolution operator $\hat{U}(t) = \Pi_{n=0}^{N-1} \exp(i\hat{H}\Delta t/\hbar)$, with Δt the chosen time step, is computed with a Chebyshev polynomial expansion method.[55–60] Calculations are performed for several initial random phase wave packets, and for a total elapsed time $t \approx 3.6$ ps split in three parts with different time steps $\Delta t_1 \approx 1.32$ fs, $\Delta t_2 \approx 26.33$ fs, and $\Delta t_3 \approx 52.66$ fs. The size of simulated graphene planes is $L_x \times L_y = 300 \times 250$ nm$^2 \sim 0.074$ μm^2 (i.e., 2.8×10^6 atoms), large enough to avoid finite-size effects while periodic boundary conditions are applied to ensure continuity of the propagation of the wave packets. In the Kubo-Greenwood formalism, the different transport regimes can be inferred from the time dependence of the diffusivity coefficient $D(E,t)$. The wave-packet velocity $v(E)$ can be extracted for instance from the short-time behavior of the diffusivity (*ballistic regime*) $D(E,t) \sim v^2(E)t$, while the elastic mean-free path $\ell_e(E)$ is estimated from the maximum of the diffusivity (*diffusive regime*) $D_{\max}(E) = 2v(E)\ell_e(E)$. The Kubo-Greenwood conductivity is given by

$$\sigma(E_F,T_F) = -\int_{-\infty}^{+\infty} dE' \frac{\partial f(E',T_F)}{\partial E'} \sigma(E',0\ \mathrm{K}), \qquad (2)$$

where E_F is the Fermi energy and $f(E,T_F)$ is the Fermi-Dirac distribution function with T_F the associated Fermi-Dirac temperature. For two-dimensional systems and at $T_F = 0$ K, the Kubo-Greenwood conductivity is therefore

$$\sigma(E_F,T_F = 0\ \mathrm{K}) = \frac{1}{4}e^2\rho(E_F) \lim_{t\to\infty} \frac{\partial}{\partial t}\Delta R^2(E_F,t). \qquad (3)$$

In these two last equations, the Fermi level (E_F) has to be thought as an energy that can be tuned with a virtual electrostatic gate, so that the transport is accessible in a large energy window around the equilibrium position of the Fermi level. However, to avoid any confusion, we set $E_F \equiv E$ in the following and reserve the notation E_F to the equilibrium Fermi energy at zero gate voltage (when the system is charge neutral). Note that we ignore the effects of screening by charge accumulation, which have been shown to be negligible in Sec. II B.

In the semiclassical transport picture, the asymptotic behavior of $\Delta R^2(E,t)$ at long time is linearly proportional to t (*diffusive regime*). Therefore, the derivative with respect to the time [Eq. (3)] can be replaced by the diffusivity coefficient $D(t) = \Delta R^2(t)/t$ in the Kubo-Greenwood conductivity formula to obtain the expression of the semiclassical conductivity

$$\sigma_{\mathrm{sc}}(E,0\ \mathrm{K}) = \tfrac{1}{4}e^2\rho(E) \lim_{t\to\infty} D(E,t), \qquad (4)$$

$$\sigma_{\mathrm{sc}}(E,0\ \mathrm{K}) = \tfrac{1}{4}e^2\rho(E)D_{\max}(E). \qquad (5)$$

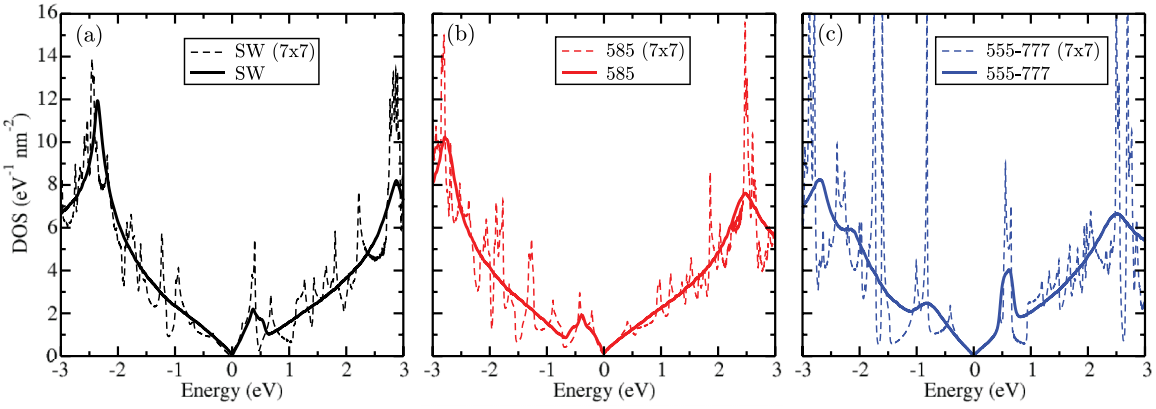

FIG. 7. (Color online) TB DOS for a 7×7 supercell (dashed lines) containing (a) one SW defect, (b) one 585 divacancy, (c) one 555-777 divacancy, i.e., $n_d \sim 1\%$, and for a large plane (thick lines) with $n_d = 1\%$ of (a) SW defects, (b) 585 divacancies, (c) 555-777 divacancies, distributed and oriented randomly.

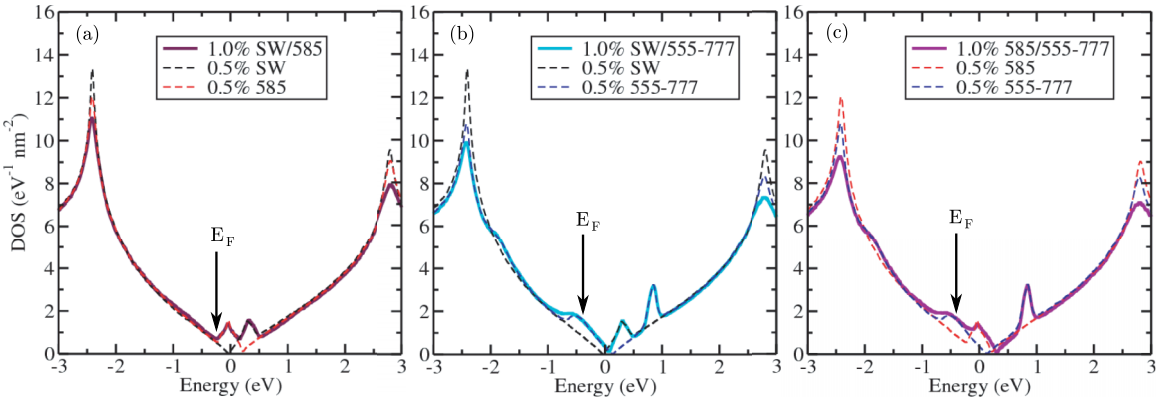

FIG. 8. (Color online) TB DOS for a large graphene plane with $n_d = 1\%$ defects (thick solid lines) of (a) SW/585, (b) SW/555-777, and (c) 585/555-777. These DOS are compared with DOS obtained with $n_d = 0.5\%$ of each defect separately (dashed lines). The position of the Fermi energy is indicated by a vertical arrow.

Finally, following the scaling theory,[61–63] the localization length $\xi(E)$ can be determined from the semiclassical transport length scales as

$$\xi(E) = \sqrt{2}\ell_e(E)\exp\left(\frac{\pi h\sigma_{\rm sc}(E,0\ {\rm K})}{2e^2}\right). \qquad (6)$$

In the quantum regime, interferences in scattering paths survive and a decrease of $D(t)$ is therefore expected (*localization regime*). A sketch in Fig. 9 illustrates the typical behavior of the diffusivity coefficient as a function of time, outlining the various possible transport regimes.

C. Semiclassical transport: Diffusive regime

The semiclassical transport regime excludes all quantum interferences effects and corresponding localization phenomena (weak and strong localization regimes). It simply captures scattering events within the diffusive regime, as derived within the self-consistent Born approximation.[66,67] Therefore, to extract the semiclassical transport length scales, the Kubo-Greenwood formalism is restricted to the diffusive regime limit, i.e., the maximum of the diffusivity coefficient $D_{\rm max}$ as illustrated in Fig. 9 (red line). In the following, the semiclassical transport properties of graphene planes containing various types and densities of structural defects will be described. First, the elastic mean-free paths will be examined, then the mobilities, and finally the semiclassical conductivities will be discussed.

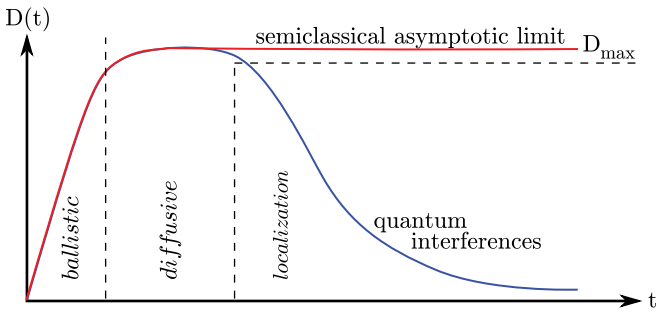

FIG. 9. (Color online) Sketch of the typical behavior of $D(t)$ showing the three possible transport regimes including the localization regime where the diffusivity decreases due to quantum interferences. In the semiclassical picture, $D(t)$ stays in the diffusive regime [i.e., $\lim_{t\to\infty} D(t) = D_{\rm max}$].

1. Mean-free path

In Fig. 10, the calculated mean-free paths are presented for graphene planes in which SW/585 defects, SW/555-777 defects, or 585/555-777 defects have been incorporated, with different defect concentrations ranging from $n_d = 0.1\%$ to 1.0%. The mean-free paths exhibit strong variations in energy, with dips associated to the defect resonance energies (peaks in the DOS). Note that from now, Fermi energy is always set to zero. The largest and fastest variation is obtained in an energy window corresponding to the 585 defect resonance energy, which appears just at the right side of the Fermi energy in case of SW/585 and 585/555-777 systems. The maximum difference in the mean-free path is about one order of magnitude. A rapid variation of the transport length scales with energy (or gate voltage) offers interesting perspectives in terms of transport (or mobility) gaps.[68] Amongst the three systems composed of mixed defects studied here, the case of 585/555-777 systems might be the most efficient one with respect to the specific needs of logic devices which require an on and an off state. The shape of the corresponding $\ell_e(E)$ function is indeed the closest to a stepwise function. For $n_d = 0.1\%$, the maximum calculated mean-free paths for all different defective systems are in the range of [60,200] nm, whereas the minimal ones lie within [2,10] nm. For $n_d \geqslant 1\%$, the mean-free paths are found to be smaller than 10 nm for any energy in the window considered here (i.e., $[-3, +3]$ eV). Finally, regarding the variation of the mean-free path with defect densities, better ratios between minimum and maximum mean-free paths are expected for defect concentrations $n_d < 0.1\%$. Unfortunately, these smaller defect concentrations are not accessible to our simulations due to computational limitations.

2. Mobility

In Fig. 11, the mobilities as a function of carrier energy [Figs. 11(a)–11(c)] and of carrier density [Figs. 11(d)–11(f)] computed with a Fermi-Dirac temperature of 300 K are illustrated. The mobility (μ) is calculated using the conventional

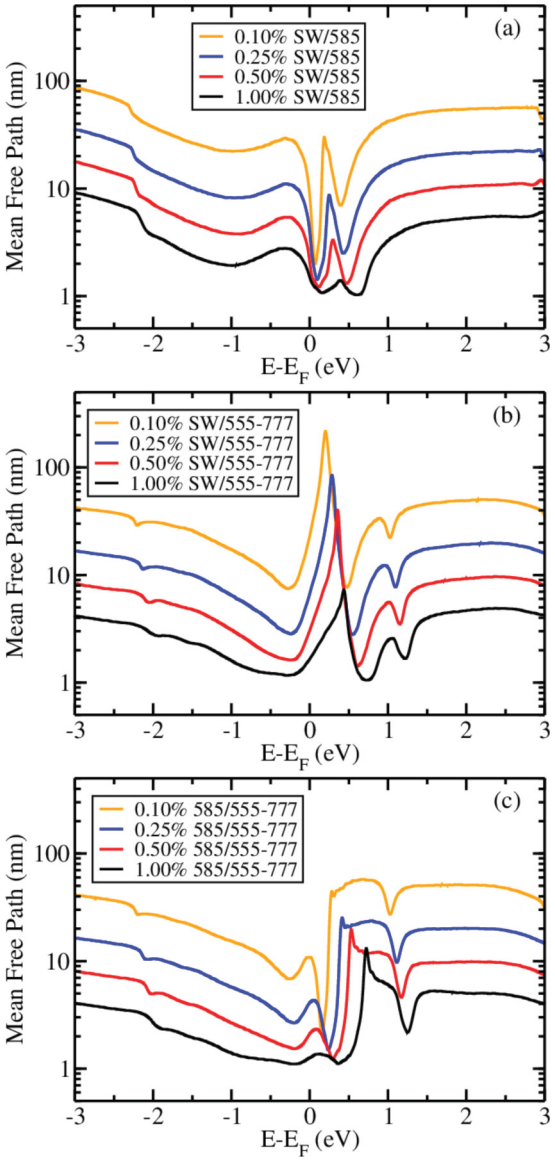

FIG. 10. (Color online) Mean-free paths in graphene planes with (a) SW/585 defects, (b) SW/555-777 defects, and (c) 585/555-777 defects, for different defect concentrations ranging from $n_d = 0.1\%$ to 1.0%.

definition $\mu(E,T_F) = \sigma_{sc}(E,T_F)/e\,n(E,T_F)$ where e is the elementary charge and $n(E,T_F)$ the charge carrier density (electrons or holes) computed by integrating the DOS from the Dirac point to the energy E. Since μ is inversely proportional to the charge carrier density (n), there is an obvious mathematical divergence of μ when n tends to zero (close to the Dirac point) as observed in Fig. 11. In each of the three cases (SW/585, SW/555-777, and 585/555-777), the p-doping character induced by divacancies is clearly illustrated by the continuous shift of the mobility peak with respect to the Fermi level as n_d increases [Figs. 11(a)–11(c)]. Some dips in the mobility are also visible even if they seem to be not as deep as for the mean-free path because the logarithm scale used in Fig. 11 run over five orders of magnitudes. The fastest variation is again obtained around the resonance energies associated to 585 defects and corresponds to a change of mobility values between two and three orders of magnitudes. For the largest defect concentration ($n_d = 1\%$), the mobility can drop below 10 cm^2 V^{-1} s^{-1} while keeping a value of a few ten thousands of cm^2 V^{-1} s^{-1} around the Dirac point. In Figs. 11(d)–11(f), the mobilities are plotted versus the electron and hole carrier densities measured with respect to the Dirac point. Therefore, the mobility peaks are all aligned. Variations with the carrier density are found to be smoother than with the carrier energy, which is due to the nonlinear dependence between n and E [$n(E) \propto E^2$]. Nevertheless, the variation of hole mobility close to the Dirac point is still rather sharp in case of 585/555-777 defects. Far away from the Dirac point, the mobility generally tends to a constant value meaning that the conductivity is linearly dependent to the charge carrier density in these regions.

3. *Semiclassical conductivity*

In Fig. 12, the semiclassical conductivities (σ_{sc}) are plotted as a function of carrier energy and density and using $T_F = 300$ K. As for mean-free paths and mobilities, the conductivities exhibit dips at resonance energies. The value of conductivity is minimal at those energies, which indicates that a minimal conductivity can be obtained for an energy different to the Dirac point. There is also a minimum value of conductivity associated to the Dirac point which is visible for Fermi-Dirac temperature equal to 0 K (although not shown here). This minimum is very sharp and thus easily broadened by the Fermi-Dirac temperature. Nevertheless, for SW/555-777 systems, this minimum associated to the Dirac point is still observable in Fig. 12(b) for $n_d = 0.1\%$ ($E \sim 0.2$ eV).

When the defect concentration increases, the conductivity reaches the semiclassical limit of minimum conductivity $\sigma_{sc}^{min} = 2\,G_0/\pi = 4e^2/\pi\,h$ (see Ref. 16 for a discussion on the minimum conductivity), leading to the progressive formation of a plateau of conductivity around the defect resonance energies. Consequently, the conductivity curves present a lot of different behaviors versus the energy. These different behaviors (constant, linear, quadratic,...) are even more obvious in Figs. 12(d)–12(f), where conductivities are plotted versus the carrier density. For instance, for $n_d = 0.1\%$, depending on the defective graphene planes and on the type of carriers, either a linear behavior can be observed (for electrons in SW/585 defective planes and in a smaller extend for electrons in SW/555-777 defective planes), or a quadratic behavior (for electrons and holes close to the Dirac point and more precisely around the defect resonances of all three types of defective planes), or again a sublinear behavior (for holes in SW/585 defective planes and electrons in 585/555-777 defective planes). For $n_d = 1.0\%$, the conductivity even displays an almost constant behavior (plateau) over a large range of carrier density since the conductivity has reached the semiclassical conductivity limit σ_{sc}^{min}. The fact that all these different behaviors for $\sigma_{sc}(n)$ are present in these defective graphene planes is an interesting observation for the current puzzling interpretation of $\sigma_{sc}(n)$.[69,70]

The semiclassical electronic transport in graphene containing various mixtures of structural defects has been investigated in this paragraph. The structural defects, which break locally the symmetry of the honeycomb lattice, have been found

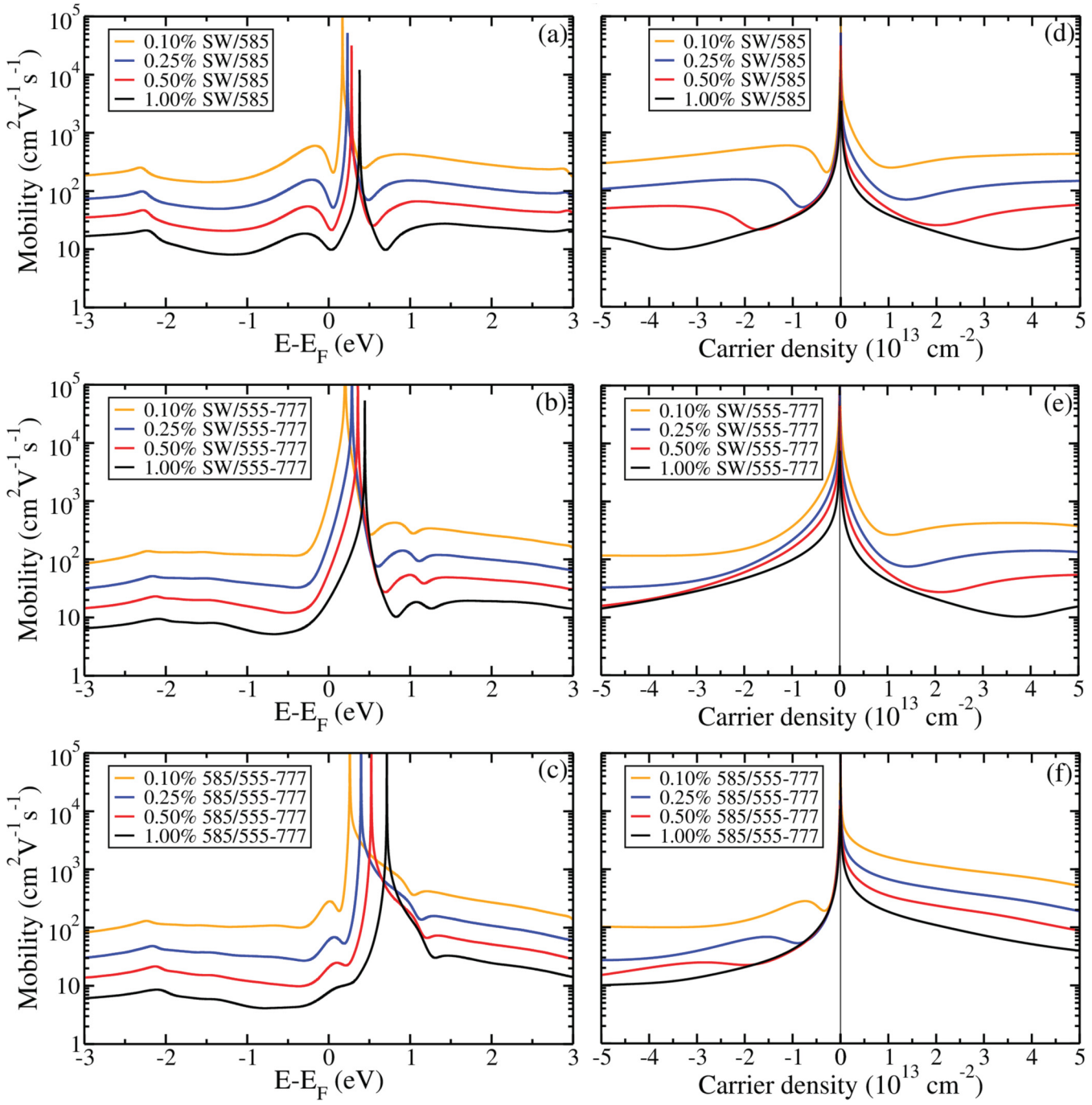

FIG. 11. (Color online) Mobilities as a function of charge carrier energy (left panels) and as a function of charge carrier density (right panels) of graphene planes with (a), (d) SW/585 defects, (b), (e) SW/555-777 defects, and (c), (f) 585/555-777 defects, for different defect concentrations ranging from $n_d = 0.1\%$ to 1.0%.

to yield to resonance scattering at specific energies. These defect resonance levels induce peaks in the DOS which increase with the defect density. These resonant states conduct systematically to a degradation of all transport properties examined (mean-free paths, mobilities, and conductivities). This degradation occurring at specific energies constitutes a fingerprint related to each type of defect separately even when several types of defects coexist in the system (provided that resonant levels are not too close in energy to overlap, which could be the case with other defects not studied here). The 585 divacancy produces a rather sharp resonance compared to the two other defects. In particular, the case of 585/555-777 defective system presents an interesting profile regarding variations of transport properties with respect to carrier energy and carrier density. Finally, large plateaus of minimum conductivity are predicted for sufficiently high concentration of defect ($n_d > 0.5\%$).

In the next section, the quantum regime of transport in such defective graphene systems will be discussed. In this transport regime, the quantum interferences in electron trajectory will

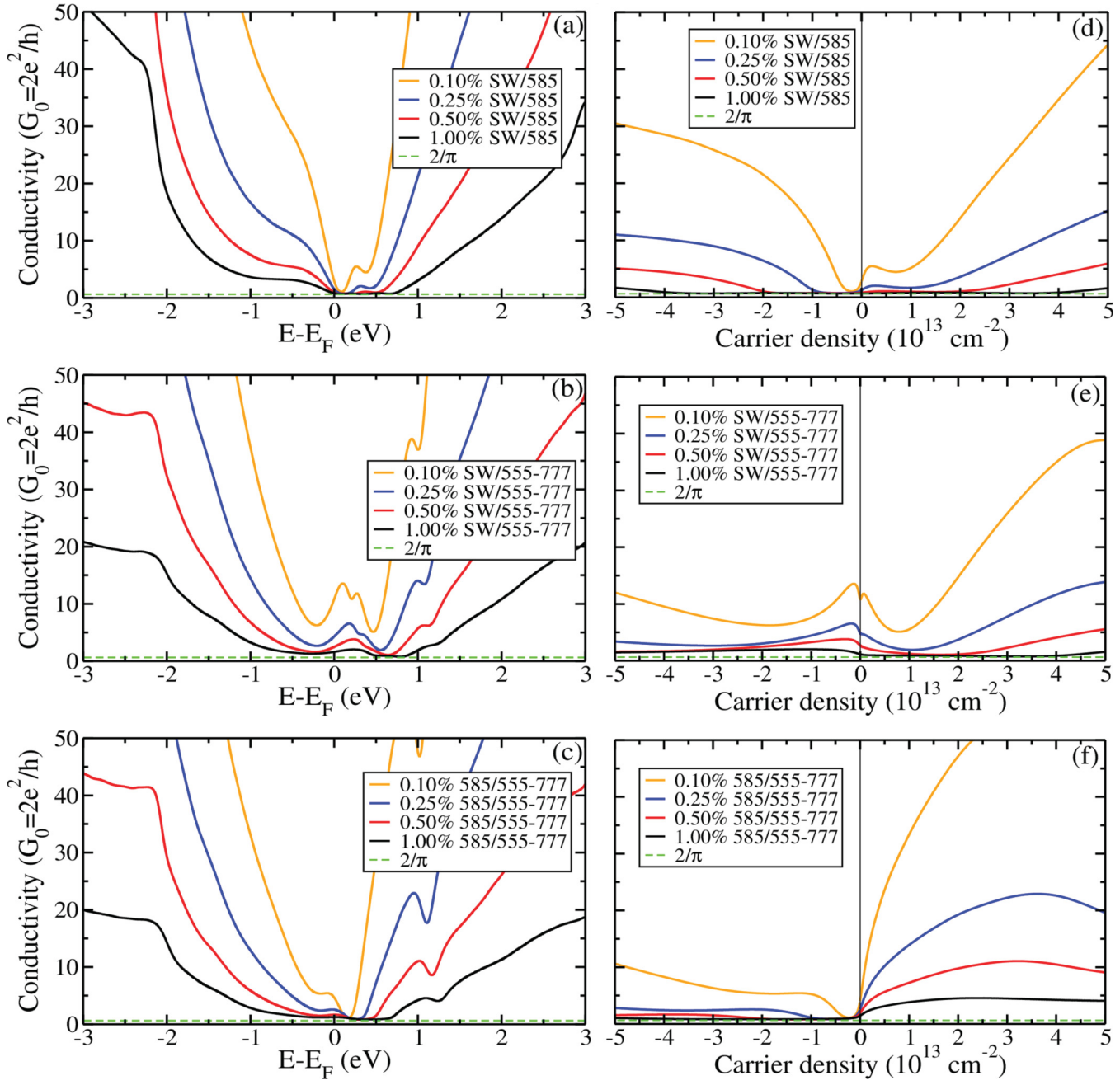

FIG. 12. (Color online) Conductivities as a function of charge carrier energy (left panels) and as a function of charge carrier density (right panels) of graphene planes with (a), (d) SW/585 defects, (b), (e) SW/555-777 defects, and (c), (f) 585/555-777 defects, for different defect concentrations ranging from $n_d = 0.1\%$ to 1.0%.

be taken into account yielding to localization phenomena and thus an additional degradation of the conductivity.

D. Quantum transport: Localization regime

In the localization transport regime, quantum interferences can yield to an enhanced probability to be backscattered. In a common picture, this effect can be viewed as constructive interferences between forward and backward electron scattering trajectories that form loops. This is possible only if the electron keeps its phase and, thus, any source of phase decoherence such as electron-phonon scattering will destroy these interferences. This is the reason why such localization effects are usually observable at low temperature only. However, in graphene the electron-phonon scattering has been found to be extremely low,[71,72] allowing the localization phenomena to occur even at room temperature. Concerning the transport quantities, the quantum interferences induce a correction which can be described theoretically through a cooperon term.[73] For a two-dimensional system, this cooperon correction yields for instance to a decrease of conductivity which scales logarithmically with the sample size (weak localization regime) for two-dimensional systems. For even stronger disordered systems, the scaling of the conductivity

exhibits an exponential decay (strong localization regime), and the electronic states become strongly localized such that the system behaves as an insulator from transport properties point of view.[74] Several theoretical and experimental studies on graphene have reported such a (semi)metal-insulator transition through an Anderson localization of electronic states, which was caused either by hydrogen atoms,[75–80] epoxy oxygen atoms,[81–83] vacancies and other structural defects,[45,51,84–86] or even noble-metal clusters.[87]

1. Diffusivity

In our real-space Kubo-Greenwood calculations, this degradation of transport quantities caused by the quantum interferences can be directly observed through the time dependence of the diffusivity coefficient. Figures 13(a)–13(c) illustrate this time dependence of normalized diffusion coefficients $[D(t)/D_{\max}]$ for four selected energies (including the Fermi energy), while Figs. 13(d)–13(f) present a 3D plot of the same quantity for a large energy window of the spectrum. The four energies selected in Figs. 13(a)–13(c) are pointed with vertical arrows in Figs. 13(d)–13(f). The decreasing of $D(t)$ clearly reveals the emergence of localization effects. This decreasing is not homogeneous in the whole spectrum but stronger at the defect resonance energies. Actually, far away from these resonance energies, the behavior of $D(t)$ at long time is a constant, which is typical of a semiclassical diffusive regime.

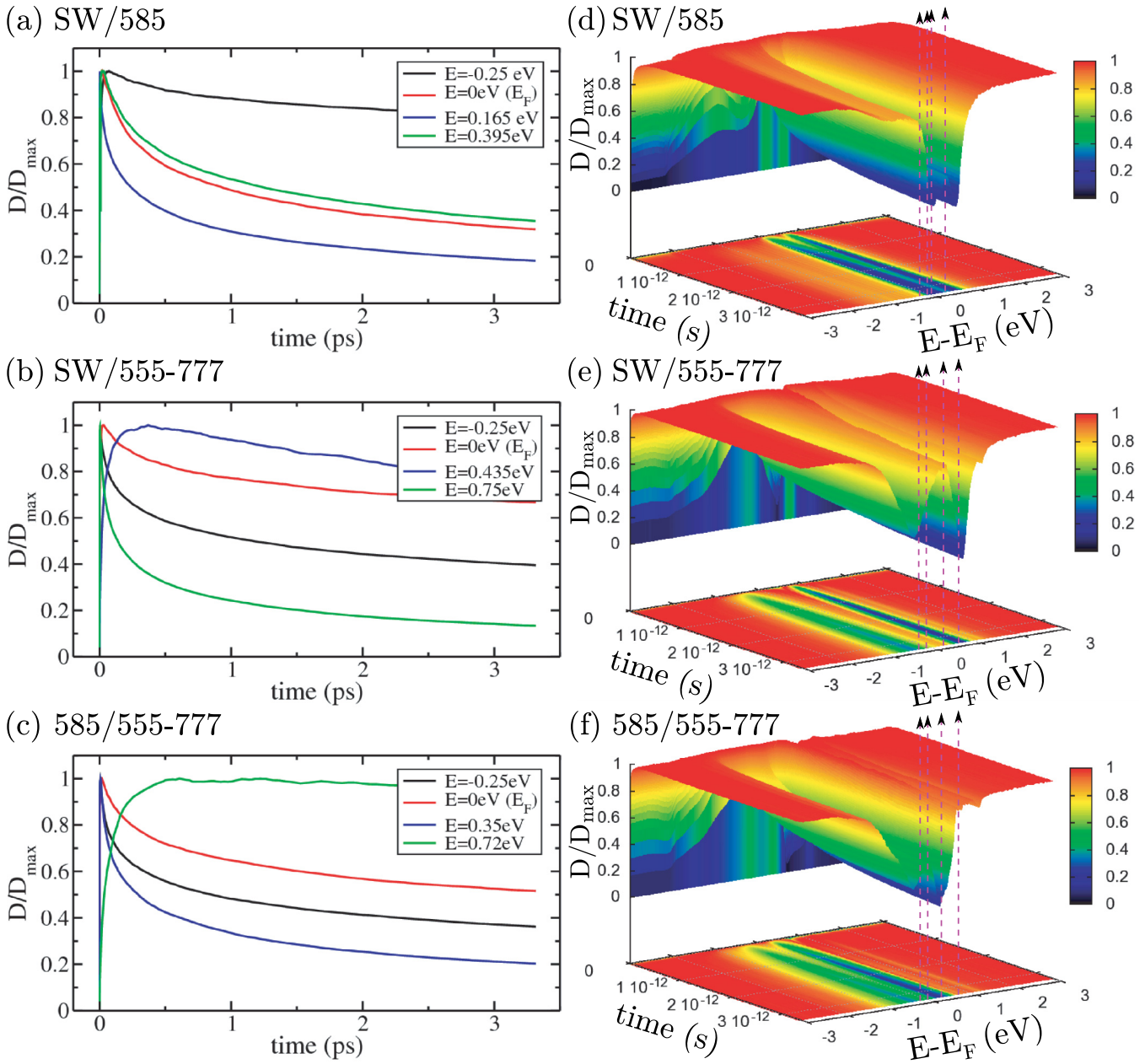

FIG. 13. (Color online) Normalized diffusivity as a function of time for four selected energies (left panels) and 3D plots as a function of time and energy (right panels) of graphene planes with (a), (d) SW/585 defects, (b), (e) SW/555-777 defects, and (c), (f) 585/555-777 defects, for a defect concentration $n_d = 1.0\%$.

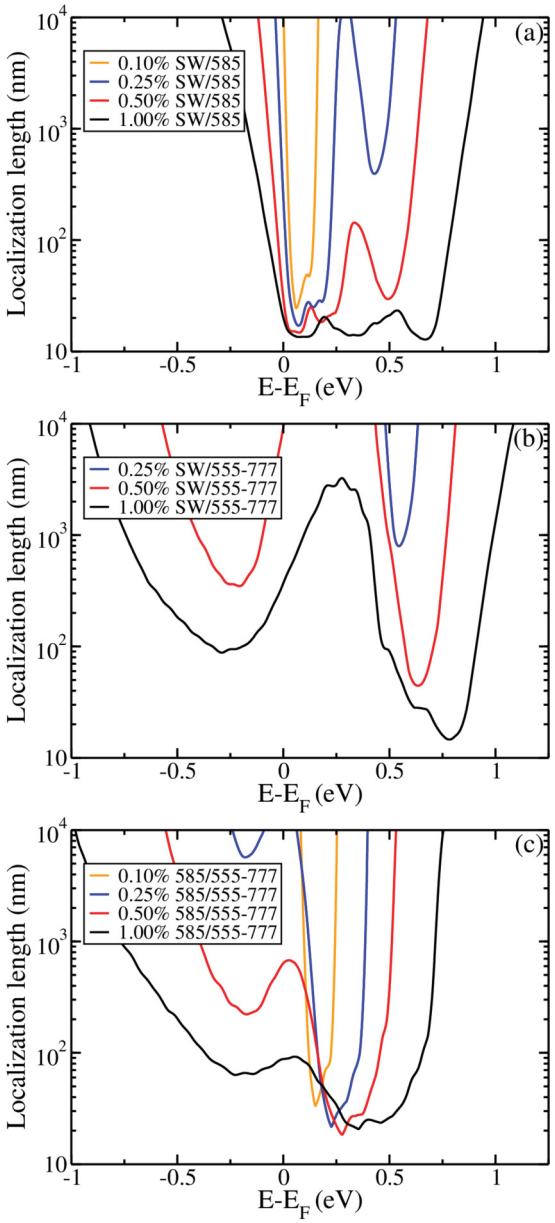

FIG. 14. (Color online) Localization lengths, evaluated using Eq. (6), in graphene planes with (a) SW/585 defects, (b) SW/555-777 defects, and (c) 585/555-777 defects, for different defect concentrations ranging from $n_d = 0.1\%$ to 1.0%.

2. Localization length

Since localization phenomena at some specific energies have been observed, the corresponding localization length (ξ) can be estimated using Eq. (6) (see Fig. 14). For the highest defect concentration (1.0%), the smallest localization lengths, obtained exactly at the defect resonance energies, are $\xi = 10$–20 nm about. At these energies, the conductivity reaches the semiclassical lower limit (i.e., σ_{sc}^{min}), and therefore, Eq. (6) becomes $\xi(E) = \sqrt{2}\ell_e(E)\exp(2) = 10.5\ell_e(E)$ with the smallest value obtained for ℓ_e being around 1 nm. Away from the resonance energies, the localization length increases very rapidly, mostly driven by the conductivity which appears in the exponential function. Such a behavior is a common feature of two-dimensional systems which makes the experimental observation of localization generally difficult even if the mean-free path is very small.

3. Extension of the real-space Kubo-Greenwood methodology

In Sec. III C, the Kubo-Greenwood methodology has been used to describe semiclassical transport properties using quantities extracted only from the diffusive regime [maximum of $D(t)$]. In the previous paragraph, even the localization lengths have been extracted from semiclassical quantities using the scaling theory of localization [Eq. (6)]. The reason why the Kubo-Greenwood formalism is usually restricted to the diffusive regime is because this is a *bulk* formalism in the sense that the framework is devoted to the description of the intrinsic properties of a material. For instance, within the Kubo-Greenwood formalism, the calculated semiclassical conductivity is an intensive quantity contrarily to the conductance which is extensive and depends on the system geometry. Hence, the Kubo-Greenwood conductivity formula is usually employed in its thermodynamic limit $t \to \infty$ [Eqs. (3) and (4)]. This infinite-time limit imposes to restrict the analysis of $D(t)$ to its asymptotic value, which can be either a constant (purely diffusive regime, $\sigma = \sigma_{sc}$) or zero (completely localized regime, $\sigma = 0$). On the contrary, the Landauer-Büttiker transport approach is better suited to describe extensive transport properties such as the conductance [$G(L)$]. In this formalism, the presence of leads introduces a finite length L of the system, which allows scaling analysis describing therefore all intermediate regimes. Even if there is *a priori* no clear definition of length in the Kubo-Greenwood approach since the system is periodic (bulk), the present real-space implementation of this transport formalism provides a complete description of the dynamics of propagation, going from the ballistic regime at very short time simulations to quasidiffusive and diffusive regimes as well as the weak and strong localization regimes at longer time. In fact, in these real-space simulations, the computed spreading of wave packets can be seen as an average time-dependent distance probed by the propagating charge carriers. To allow a scaling analysis within the real-space Kubo-Greenwood approach, the introduction of a characteristic length scale $L(t)$ defined as the diameter of a fictitious circle formed by the spreading of wave packets is therefore proposed:

$$L(E,t) = 2\sqrt{\Delta R^2(E,t)}. \tag{7}$$

This new approach, which gives access to length-dependent transport quantities and allows us to describe more in details the localization phenomena, will be verified and justified in the following by comparing the results with the predictions of the scaling theory of localization. Before that, the definition of the diffusion coefficient $D(t)$ has to be reexamined.

As pointed out by Eq. (3), the general definition of the diffusion coefficient is given by $D(t) = \frac{\partial}{\partial t}\Delta R^2(t)$. In the diffusive regime, the quadratic spreading of wave packets being linearly proportional to the time [$\Delta R^2(t) \propto t$], its first derivative reduces exactly to the constant value $D(t) = \Delta R^2(t)/t$. For numerical convenience, it is more efficient to use the definition $D(t) = \Delta R^2(t)/t$. Indeed, the first derivative is more computationally demanding and its numerical evaluation can produce large fluctuations from which it is

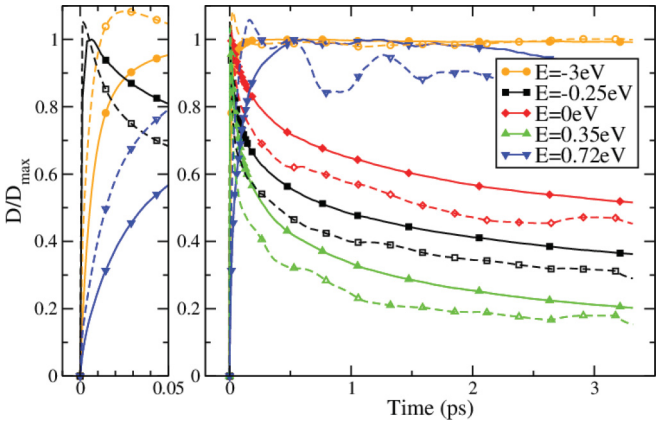

FIG. 15. (Color online) Normalized diffusivity $D(t)$ in graphene planes with 1.0% of 585/555-777 defects, as a function of time for five selected energies. Solid lines are obtained with $\Delta R^2(t)/t$, whereas dashed lines are obtained with $\frac{\partial}{\partial t}\Delta R^2(t)$. Both expressions are divided by $D_{\max}$ found for $\Delta R^2(t)/t$.

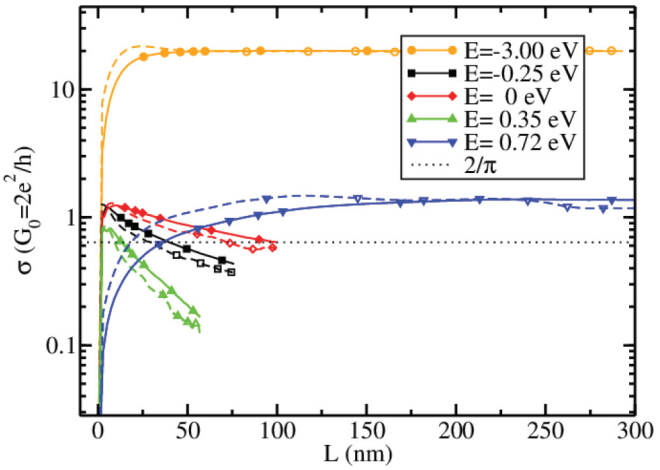

FIG. 16. (Color online) Quantum conductivity $\sigma(E,L)$ in graphene planes with 1.0% of 585/555-777 defects, as a function of length for five selected energies. We use $D(t) = \Delta R^2(t)/t$ (solid lines) and $D(t) = \frac{\partial}{\partial t}\Delta R^2(t)$ (dashed lines) for computing $\sigma(L)$. The horizontal dotted line gives the semiclassical limit $\sigma_{\rm sc}^{\rm min} = 2/\pi\ G_0 = 4e^2/\pi\ h$.

difficult to extract semiclassical transport properties. In the localization regime, since $D(t)$ is no more a constant, the general definition $D(t) = \frac{\partial}{\partial t}\Delta R^2(t)$ should be used. However, although using $D(t) = \Delta R^2(t)/t$ is in principle incorrect in the localization regime, it is nevertheless interesting to compare the two definitions. In Fig. 15, the diffusivity coefficient is plotted using either $D(t) = \Delta R^2(t)/t$ (solid lines) or $D(t) = \frac{\partial}{\partial t}\Delta R^2(t)$ (dashed lines). For sake of comparison, both definitions are normalized with the same value of maximum of diffusivity ($D_{\max}$) found for $D(t) = \Delta R^2(t)/t$. For an energy far from the resonance energies, e.g., $E = -3$ eV for which no localization effects are observed, the two curves (solid and dashed lines) are almost superimposed. Both evaluations of $D(t)$ at long time, deep in the diffusive regime, give thus the same constant value. The only difference is a bump obtained for the diffusivity evaluated with the numerical derivative. This bump appears at the transition between the ballistic and the diffusive regimes. In principle, there is no reason to observe a decrease of $D(t)$ in a purely diffusive regime as shown in Fig. 9. This bump is thus just an artifact produced by small numerical errors in $\Delta R^2(t)$ then enhanced by its first derivative calculation.[65] In the localization regime, which is clearly predicted for energies $E = -0.25$, 0,and 0.35eV, Fig. 15 shows that the diffusivity computed with $D(t) = \Delta R^2(t)/t$ overestimates the one derived with $D(t) = \frac{\partial}{\partial t}\Delta R^2(t)$. Nevertheless, the overestimation in the localization regime being almost constant with increasing time, the general behavior is still correct when $D(t)$ is evaluated with $D(t) = \Delta R^2(t)/t$. Moreover, the curves obtained with that definition are much smoother. The definition $D(t) = \Delta R^2(t)/t$ could therefore be conserved even in the localization regime, keeping in mind that it slightly overestimates the true value. With such a clarification for the definition of diffusivity in the localization regime, the scaling analysis of the conductivity in the quantum regime can be performed.

By using Eq. (7), transport quantities can be expressed as a function of length (L) instead of as a function of time (t). To check the validity of this presumed definition of L, the scaling of the conductivity can be compared to the predictions of the scaling theory. In particular, this theory predicts the length dependence of quantum corrections (cooperon term) to the conductivity due to localization effects. For two-dimensional systems, these corrections are logarithmic[73] and read as

$$\sigma(E,L) = \sigma_{\rm sc}(E) - \frac{2e^2}{h\pi}\ln\left(\frac{L}{\sqrt{2}\ell_e(E)}\right) = \sigma_{\rm sc}(E) - \frac{G_0}{\pi}\ln\left(\frac{L}{\sqrt{2}\ell_e(E)}\right). \quad (8)$$

In Fig. 16, using Eq. (7), the quantum conductivity as a function of length [$\sigma(L)$] is presented employing either $D(t) = \Delta R^2(t)/t$ (solid lines) or $D(t) = \frac{\partial}{\partial t}\Delta R^2(t)$ (dashed lines). The horizontal dotted line denotes $\sigma_{\rm sc}^{\rm min}$. As for the diffusivity (Fig. 15), both definitions of $D(t)$ lead to similar conductivity curves, but the use of $D(t) = \Delta R^2(t)/t$ produces smoother curves and a slight overestimation in the localization regime. Localization effects are absent for $E = -3$ eV as evidenced by the saturation of $\sigma(L)$ to its semiclassical asymptotic constant value $\sigma_{\rm sc}$. For other energies (especially for $E = -0.25$, 0,and 0.35 eV), localization effects induce a decreasing of quantum conductivity with increasing length. The semiclassical value $\sigma_{\rm sc}$ [which is maximum of $\sigma(L) \equiv \sigma_{\max}$] is always found to be greater than $\sigma_{\rm sc}^{\rm min} = 2G_0/\pi$, while quantum conductivity can decrease below such a value for sufficiently long lengths and for energies close enough to the defect resonance energies. Finally, Fig. 16 exhibits a maximum computed length which is different for each energy. Indeed, as explained by the length scale [Eq. (7)], which is energy dependent for a fixed total elapsed time, the length probed by the spreading of wave packets can be different.

In Fig. 17, the validity of the definition of the length L [Eq. (7)] is checked by scrutinizing if the quantum conductivity decay (solid lines) follows a logarithmic behavior as predicted by the scaling theory [Eq. (8)]. The dotted lines correspond to Eq. (8). The dashed-dotted lines correspond to a modified version of Eq. (8) in which a new length scale ($l_{\rm diff}$) has been

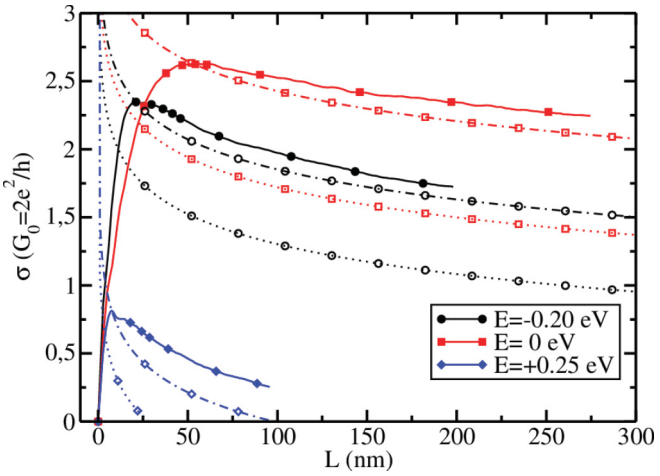

FIG. 17. (Color online) Quantum conductivity in graphene planes with 0.25% of 585/555-777 defects, as a function of length and for three selected energies. Solid lines are obtained using $D(t) = \Delta R^2(t)/t$. The dotted lines are obtained using Eq. (8) the and dashed-dotted lines using Eq. (9) in which the new length scale l_{diff} has been introduced.

introduced replacing the mean-free path:

$$\sigma(E,L) = \sigma_{\text{sc}}(E) - \frac{G_0}{\pi} \ln\left(\frac{L}{l_{\text{diff}}(E)}\right) \tag{9}$$

with l_{diff} defined as the length corresponding to σ_{max}.

In the review of Lee and Ramakrishnan,[61] the equation of weak localization correction in the scaling theory is derived using the mean-free path as the characteristic length scale of the diffusive regime. According to this definition, when the length L is equal to the mean-free path ℓ_e, the conductivity should be maximal, which corresponds to the semiclassical conductivity ($\sigma_{\text{sc}} \equiv \sigma_{\text{max}}$), and for $L > \ell_e$ weak localization should develop. In contrast, using Eq. (7), the obtained semiclassical conductivity (or σ_{max}) occurs at a length scale different from ℓ_e. For instance in Fig. 17, for an energy $E = 0$ eV ($E = E_F$), the maximum of conductivity occurs at $L = l_{\text{diff}} \sim 53$ nm, which is about 10 times greater than the mean-free path computed at this energy ($\ell_e \sim 4$ nm). Therefore, the definition of length Eq. (7) might be questioned and argued to be misleading. But, considering the scaling in time for which there is no ambiguity, there is also a factor of 10 between the calculated mean scattering time τ and the time t for which the diffusivity coefficient reaches its maximum value. Actually, in a semiclassical picture, this is consistent with the fact that to reach completely the diffusive regime [saturation of $D(t)$], the charge carriers need to encounter several scattering events which correspond thus to a total traveling distance of a few times the mean-free path. Likewise, the charge carriers need several scattering events before the weak localization corrections start to present a clear effect. Indeed, these corrections are due to constructive interferences between forward and backward scattering paths, which form loop trajectories. The shortest loop trajectory is at least two times the mean-free path in a semiclassical picture. The introduction of an additional length scale l_{diff} is therefore meaningful for the interpretation of such quantum corrections. In Fig. 17, it is obvious that the conductivity decay follows the logarithmic behavior predicted by Eq. (8). However, using the mean-free path as a characteristic length scale in the formula does not allow to fit $\sigma(L)$. On the contrary, Eq. (9) allows us to more correctly predict the scaling of the conductivity and therefore to extrapolate to lengths L longer than the ones computed. As a consequence, the localization length ξ can be extracted with a better precision by replacing the mean-free path ℓ_e by the diffusion length l_{diff}. Indeed, ξ can be evaluated as the length L for which the conductivity is equal to zero or equivalently for which the weak localization corrections are equal to the semiclassical conductivity:

$$\sigma(E, L = \xi) = 0 = \sigma_{\text{sc}}(E) - \frac{G_0}{\pi} \ln\left(\frac{L}{l_{\text{diff}}(E)}\right),$$
$$\xi(E) = l_{\text{diff}}(E) \exp\left(\frac{\pi \sigma_{\text{sc}}(E)}{G_0}\right). \tag{10}$$

Compared to Eq. (6), the localization lengths calculated using Eq. (10) are roughly 10 times longer for weak localization regime and about 4–5 times longer for stronger localization regime. For instance, in Fig. 17 for an energy $E = 0.25$ eV, which corresponds exactly to the resonance of 585 divacancy and for which the localization effects are stronger, $\xi \sim 25$ nm obtained with Eq. (6) and $\xi \sim 100$ nm estimated with Eq. (10). Note, however, that in case of strong localization effects such as $E = 0.25$ eV in Fig. 17 and for higher defect densities such as 1% (not shown here), there is a deviance between the logarithmic decay predicted by scaling theory for the weak localization corrections and the actual computed quantum conductivities. As already reported recently in Ref. 83, in such strong localization case, the weak localization corrections are no more suitable and an exponential decay has to be used to describe the scaling of $\sigma(L)$, which results in a long tail corresponding to evanescent modes. Finally, in very strong localization regime, the localization length could alternatively be evaluated from the long-time saturation of the quadratic spreading[64] as

$$\xi(E) = \lim_{t \mapsto \infty} 2\sqrt{\Delta R^2(E,t)} = \lim_{t \mapsto \infty} L(E,t). \tag{11}$$

Unfortunately, a complete saturation of the quadratic spreading has never been observed in our simulations for the total elapsed time computed.

IV. CONCLUSION

In conclusion, the electronic and transport properties of graphene containing structural defects such as SW, 585, and 555-777 divacancies have been investigated theoretically. Using *ab initio* techniques, the geometry and the electronic band structures of single defects in a supercell have been computed. The *ab initio* relaxed atomic positions and electronic defect potentials have been employed to build accurate TB models for each individual structural defect. Comparisons between *ab initio* and TB band structures and DOS have displayed a good agreement. The elaborated TB models have then been employed to compute DOS of large graphene planes containing randomly distributed structural defects of various natures and concentrations. The comparison of these DOS with the DOS obtained for the supercell have evidenced the smoothening effect of the randomness character in distribution

and orientation of defects at a mesoscopic scale. In addition, the computed TB-DOS of graphene containing a mixture of defects have illustrated that defect-induced resonant peaks can be assigned to individual defects separately, demonstrating that those resonances constitute a fingerprint of each structural defect. Afterwards, using a Kubo-Greenwood method, the transport properties have been investigated. The computed semiclassical transport quantities, such as mean-free path, mobility, and conductivity have exhibited systematic degradations around defect resonance energies. In particular, it has been predicted that a minimum conductivity ($\sigma_{sc}^{min} = 4e^2/\pi\ h$) can be obtained at an energy different than Dirac point, and that plateau of minimum conductivity are formed when increasing the defect density. Finally, a detailed analysis of the diffusivity deep into the localization regime has allowed us to extend the use of the Kubo-Greenwood method to predict length dependence of the quantum conductivity [$\sigma(L)$]. As expected by the scaling theory, σ exhibits a logarithmic decay with increasing lengths around defect resonance energies due to localization phenomena. An Anderson insulating behavior is thus anticipated for graphene with 1% of structural defect and associated localization lengths are expected to be in the order of a few tens of nanometers. However, localization effects are not observed in the whole spectrum, but only around defect resonance energies, thus complicating its experimental detection. Transport measurements would thus require an efficient electrostatic gate to probe a larger window of the spectrum and to align Fermi energy with these defect resonance energies. Additionally, transport characterization with different sizes of graphene samples exposed to the same amount of structural defects could be conducted in order to perform scaling analysis of the conductivity. Alternatively, magnetotransport experiments on a fixed size sample could also reveal localization phenomena induced by structural defects as well as low-temperature transport measurements, which should evidence a variable range hopping behavior.

ACKNOWLEDGMENTS

J.-C.C. and A.L., X.D., and S.M.-M.D. acknowledge financial support from the F.R.S.-FNRS of Belgium, the FRIA, and the EPSRC (Grant No. EP/G055904/1), respectively. Parts of this work are connected to the ARC Graphene Nano-electromechanics (Grant No. 11/16-037) sponsored by the Communauté Française de Belgique, to the European Union through the ETSF e-I3 project (Grant No. 211956), and to the NANOSIM-GRAPHENE Project (Project No. ANR-09-NANO-016-01). Computational resources have been provided by the CISM of the Université Catholique de Louvain (UCL).

[1] K. S. Novoselov, A. K. Geim, S. V. Morozov, D. Jiang, Y. Zhang, S. V. Dubonos, I. V. Grigorieva, and A. A. Firsov, Science **306**, 666 (2004).
[2] K. S. Novoselov, A. K. Geim, S. V. Morozov, D. Jiang, M. I. Katsnelson, I. V. Grigorieva, S. V. Dubonos, and A. A. Firsov, Nature (London) **438**, 197 (2005).
[3] A. K. Geim and K. S. Novoselov, Nat. Mater. **6**, 183 (2007).
[4] K. S. Novoselov, Rev. Mod. Phys. **83**, 837 (2011).
[5] Y. Zhang, Y.-W. Tan, H. L. Stormer, and P. Kim, Nature (London) **438**, 201 (2005).
[6] X. Wu, X. Li, Z. Song, C. Berger, and W. A. de Heer, Phys. Rev. Lett. **98**, 136801 (2007).
[7] F. V. Tikhonenko, A. A. Kozikov, A. K. Savchenko, and R. V. Gorbachev, Phys. Rev. Lett. **103**, 226801 (2009).
[8] F. Ortman, A. Cresti, G. Montambaux, and S. Roche, Eur. Phys. Lett. **94**, 47006 (2011).
[9] K. Bolotin, K. Sikes, Z. Jiang, M. Klima, G. Fudenberg, J. Hone, P. Kim, and H. L. Stormer, Solid State Commun. **146**, 351 (2008).
[10] F. Miao, S. Wijeratne, Y. Zhang, U. C. Coskun, W. Bao, and C. N. Lau, Science **317**, 1530 (2007).
[11] F. Xia, D. B. Farmer, Y.-M. Lin, and P. Avouris, Nano Lett. **10**, 715 (2010).
[12] A. V. Krasheninnikov and F. Banhart, Nat. Mater. **6**, 723 (2007).
[13] J.-C. Charlier, X. Blase, and S. Roche, Rev. Mod. Phys. **79**, 677 (2007).
[14] K. Suenaga, H. Wakabayashi, M. Koshino, Y. Sato, K. Urita, and S. Iijima, Nat. Nanotechnol. **2**, 358 (2007).
[15] M. T. Lusk, D. T. Wu, and L. D. Carr, Phys. Rev. B **81**, 155444 (2010).
[16] A. Cresti, N. Nemec, B. Biel, G. Niebler, F. Triozon, G. Cuniberti, and S. Roche, Nano Res. **1**, 361 (2008).
[17] A. Lherbier, X. Blase, Y. M. Niquet, F. Triozon, and S. Roche, Phys. Rev. Lett. **101**, 036808 (2008).
[18] B. Wang and S. T. Pantelides, Phys. Rev. B **83**, 245403 (2011).
[19] C. Gómez-Navarro, P. J. De Pablo, J. Gómez-Herrero, B. Biel, F. J. Garcia-Vidal, A. Rubio, and F. Flores, Nat. Mater. **4**, 534 (2005).
[20] B. Biel, F. J. Garcia-Vidal, A. Rubio, and F. Flores, Phys. Rev. Lett. **95**, 266801 (2005).
[21] J.-H. Chen, W. G. Cullen, C. Jang, M. S. Fuhrer, and E. D. Williams, Phys. Rev. Lett. **102**, 236805 (2009).
[22] F. Banhart, J. Kotakoski, and A. V. Krasheninnikov, ACS Nano **5**, 26 (2011).
[23] J. Kotakoski, A. V. Krasheninnikov, U. Kaiser, and J. C. Meyer, Phys. Rev. Lett. **106**, 105505 (2011).
[24] E. Cockayne, G. M. Rutter, N. P. Guisinger, J. N. Crain, P. N. First, and J. A. Stroscio, Phys. Rev. B **83**, 195425 (2011).
[25] E. Cockayne, Phys. Rev. B **85**, 125409 (2012).
[26] N. Leconte, D. Soriano, S. Roche, P. Ordejón, J.-C. Charlier, and J. J. Palacios, ACS Nano **5**, 3987 (2011).
[27] A. J. Stone and D. J. Wales, Chem. Phys. Lett. **128**, 501 (1986).
[28] J. Ma, D. Alfè, A. Michaelides, and E. Wang, Phys. Rev. B **80**, 033407 (2009).
[29] D. Huertas-Hernando, F. Guinea, and A. Brataas, Phys. Rev. B **74**, 155426 (2006).
[30] G.-D. Lee, C. Z. Wang, E. Yoon, N.-M. Hwang, D.-Y. Kim, and K. M. Ho, Phys. Rev. Lett. **95**, 205501 (2005).
[31] Y. Kim, J. Ihm, E. Yoon, and G.-D. Lee, Phys. Rev. B **84**, 075445 (2011).
[32] J. C. Meyer, C. Kisielowski, R. Erni, M. D. Rossell, M. F. Crommie, and A. Zettl, Nano Lett. **8**, 3582 (2008).
[33] M. M. Ugeda, I. Brihuega, F. Hiebel, P. Mallet, J.-Y. Veuillen, J. M. Gómez-Ródriguez, and F. Ynduráin, Phys. Rev. B **85**, 121402(R) (2012).

[34]J. M. Soler, E. Artacho, J. D. Gale, A. Garcia, J. Junquera, P. Ordejon, and D. Sanchez-Portal, J. Phys.: Condens. Matter **14**, 2745 (2002).
[35]D. M. Ceperley and B. J. Alder, Phys. Rev. Lett. **45**, 566 (1980).
[36]J. P. Perdew and A. Zunger, Phys. Rev. B **23**, 5048 (1981).
[37]N. Troullier and J.-L. Martins, Phys. Rev. B **43**, 1993 (1991).
[38]E. Artacho, D. Sánchez-Portal, P. Ordejón, A. García, and J. M. Soler, Phys. Status Solidi B **215**, 809 (1999).
[39]F. Libisch, S. Rotter, and J. Burgdörfer, arXiv:1102.3848.
[40]E. McCann, K. Kechedzhi, V. I. Fal'ko, H. Suzuura, T. Ando, and B. L. Altshuler, Phys. Rev. Lett. **97**, 146805 (2006).
[41]M. Mucha-Kruczyński, O. Tsyplyatyev, A. Grishin, E. McCann, V. I. Fal'ko, A. Bostwick, and E. Rotenberg, Phys. Rev. B **77**, 195403 (2008).
[42]S. Y. Zhou, D. A. Siegel, A. V. Fedorov, and A. Lanzara, Phys. E (Amsterdam) **40**, 2642 (2008).
[43]A. H. Castro Neto, F. Guinea, N. M. R. Peres, K. S. Novoselov, and A. K. Geim, Rev. Mod. Phys. **81**, 109 (2009).
[44]S. Dubois, A. Lherbier, A. Botello-Mendez, J.-C. Charlier (unpublished).
[45]A. Lherbier, Simon M.-M. Dubois, X. Declerck, S. Roche, Y. M. Niquet, and J.-C. Charlier, Phys. Rev. Lett. **106**, 046803 (2011).
[46]R. Haydock, V. Heine, and M. J. Kelly, J. Phys. C: Solid State Phys. **8**, 2591 (1975).
[47]The same broadening parameter (10 meV) has been used in both DOS calculations.
[48]J. P. Robinson, H. Schomerus, L. Oroszlány, and V. I. Fal'ko, Phys. Rev. Lett. **101**, 196803 (2008).
[49]T. O. Wehling, S. Yuan, A. I. Lichtenstein, A. K. Geim, and M. I. Katsnelson, Phys. Rev. Lett. **105**, 056802 (2010).
[50]A. Mesaros, S. Papanikolaou, C. F. J. Flipse, D. Sadri, and J. Zaanen, Phys. Rev. B **82**, 205119 (2010).
[51]G. Trambly de Laissardière and D. Mayou, Mod. Phys. Lett. B **25**, 1019 (2011).
[52]A. Lherbier, S. Roche, O. A. Restrepo, Y. M. Niquet, A. Decorte, and J.-C. Charlier (unpublished).
[53]V. Kapko, D. A. Drabold, and M. F. Thorpe, Phys. Status Solidi B **247**, 1197 (2010).
[54]E. Holmström, J. Fransson, O. Eriksson, R. Lizárraga, B. Sanyal, S. Bhandary, and M. I. Katsnelson, Phys. Rev. B **84**, 205414 (2011).
[55]S. Roche and D. Mayou, Phys. Rev. Lett. **79**, 2518 (1997).
[56]D. Mayou and S. Khanna, J. Phys. I **5**, 1199 (1995).
[57]D. Mayou, Europhys. Lett. **6**, 549 (2007).
[58]F. Triozon, J. Vidal, R. Mosseri, and D. Mayou, Phys. Rev. B **65**, 220202 (2002).
[59]S. Roche, Phys. Rev. B **59**, 2284 (1999).
[60]H. Ishii, F. Triozon, N. Kobayashi, K. Hirose, and S. Roche, C. R. Phys. **10**, 283 (2009).
[61]P. A. Lee and T. V. Ramakrishnan, Rev. Mod. Phys. **57**, 287 (1985).
[62]P. A. Lee and D. S. Fisher, Phys. Rev. Lett. **47**, 882 (1981).
[63]F. Evers and A. D. Mirlin, Rev. Mod. Phys. **80**, 1355 (2008).
[64]F. Triozon, S. Roche, and D. Mayou, RIKEN Rev. **29**, 73 (2000).
[65]This also explains why the use of the same value of $D_{\max}$ has been preferred to normalize the two equations in order to clearly see this spurious effect.
[66]N. H. Shon and T. Ando, J. Phys. Soc. Jpn. **67**, 2421 (1998).
[67]T. Ando, Int. J. Mod. Phys. B **21**, 1113 (2007).
[68]S. Roche, B. Biel, A. Cresti, and F. Triozon, Phys. E (Amsterdam) **44**, 960 (2012).
[69]T. Stauber, N. M. R. Peres, and F. Guinea, Phys. Rev. B **76**, 205423 (2007).
[70]J. Yan and M. S. Fuhrer, Phys. Rev. Lett. **107**, 206601 (2011).
[71]J. H. Chen, C. Jang, S. Xia, M. Ishigami, and M. S. Fuhrer, Nat. Nanotechnol. **3**, 206 (2008).
[72]S. V. Morozov, K. S. Novoselov, M. I. Katsnelson, F. Schedin, D. Elias, J. A. Jaszczak, and A. K. Geim, Phys. Rev. Lett. **100**, 016602 (2008).
[73]E. Akkermans and G. Montambaux, *Mesoscopic Physics of Electrons and Photons* (Cambridge University Press, Cambridge, UK, 2007).
[74]A. Lherbier, B. Biel, Y. M. Niquet, and S. Roche, Phys. Rev. Lett. **100**, 036803 (2008).
[75]J. Bang and K. J. Chang, Phys. Rev. B **81**, 193412 (2010).
[76]Y. V. Skrypnyk and V. M. Loktev, Phys. Rev. B **83**, 085421 (2011).
[77]G. Schubert and H. Fehske, Phys. Rev. Lett. **108**, 066402 (2012).
[78]R. Grassi, T. Low, and M. Lundstrom, Nano Lett. **11**, 4574 (2011).
[79]D. C. Elias, R. R. Nair, T. M. G. Mohiuddin, S. V. Morozov, P. Blake, M. P. Halsall, A. C. Ferrari, D. W. Boukhvalov, M. I. Katsnelson, A. K. Geim, and K. S. Novoselov, Science **323**, 610 (2009).
[80]A. Bostwick, J. L. McChesney, K. V. Emtsev, T. Seyller, K. Horn, S. D. Kevan, and E. Rotenberg, Phys. Rev. Lett. **103**, 056404 (2009).
[81]N. Leconte, J. Moser, P. Ordejón, H. Tao, A. Lherbier, A. Bachtold, F. Alsina, C. M. Sotomayor Torres, J.-C. Charlier, and S. Roche, ACS Nano **4**, 4033 (2010).
[82]J. Moser, H. Tao, S. Roche, F. Alsina, C. M. Sotomayor Torres, and A. Bachtold, Phys. Rev. B **81**, 205445 (2010).
[83]N. Leconte, A. Lherbier, F. Varchon, P. Ordejón, S. Roche, and J.-C. Charlier, Phys Rev. B **84**, 235420 (2011).
[84]A. Uppstu, K. Saloriutta, A. Harju, M. Puska, and A.-P. Jauho, Phys. Rev. B **85**, 041401(R) (2012).
[85]J. Haskins, A. Kinaci, C. Sevik, H. Sevinçli, G. Cuniberti, and T. Çağin, ACS Nano **5**, 3779 (2011).
[86]S. Wu and F. Liu, arXiv:1001.2057.
[87]W. Li, Y. He, L. Wang, G. Ding, Z-.Q. Zhang, R. W. Lortz, P. Sheng, and N. Wang, Phys. Rev. B **84**, 045431 (2011).